



# Hierarchical 2D to 3D micro/nano-histology of human dental caries lesions using light, X-ray and electron microscopy

Cyril Besnard<sup>a,\*</sup>, Ali Marie<sup>a</sup>, Petr Buček<sup>b</sup>, Sisini Sasidharan<sup>a</sup>, Robert A. Harper<sup>c</sup>, Shashidhara Marathe<sup>d</sup>, Kaz Wanelik<sup>d</sup>, Gabriel Landini<sup>c</sup>, Richard M. Shelton<sup>c</sup>, Alexander M. Korsunsky<sup>a</sup>

<sup>a</sup> MBLEM, Department of Engineering Science, University of Oxford, Parks Road, Oxford, Oxfordshire OX1 3PJ, UK

<sup>b</sup> TESCAN-UK Ltd., Wellbrook Court, Girton, Cambridge CB3 0NA, UK

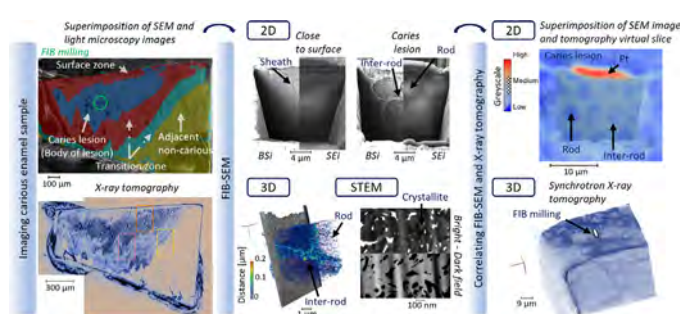
<sup>c</sup> School of Dentistry, University of Birmingham, 5 Mill Pool Way, Edgbaston, Birmingham, West Midlands B5 7EG, UK

<sup>d</sup> Diamond Light Source Ltd., Didcot, Oxfordshire OX11 0DE, UK

## HIGHLIGHTS

- Nano/macro-histological characterisation of hierarchical structure of human carious enamel performed with various techniques.
- Correlative imaging analysis using light microscopy, SEM, FIB and X-ray tomography conducted at different scales.
- Qualitative and quantitative 2D and 3D characterisation of the demineralisation of enamel carried out in key zones of carious enamel.
- Significant difference in the demineralisation of enamel in the carious lesion and in the surface zone revealed.

## GRAPHICAL ABSTRACT



## ARTICLE INFO

### Article history:

Received 2 April 2022

Revised 21 May 2022

Accepted 3 June 2022

Available online 8 June 2022

### Keywords:

Correlative imaging

Human carious enamel

Light microscopy

FIB-S(T)EM

Image analysis 2D/3D

Synchrotron X-ray tomography

## ABSTRACT

Dental caries is a widespread disease that proceeds by damaging superficial tooth enamel by heterogeneous dissolution. Conventional histology identifies different zones within carious lesions by their optical appearance, but fails to quantify the underlying nanoscale structural changes as a function of specific location, impeding better understanding of the demineralisation process. We employ detailed collocation analysis using different imaging modalities, resolutions and fields of view. Focused ion beam-scanning electron microscopy (FIB-SEM) reveals subsurface 3D nanostructure within milled micro-sized volumes, whilst X-ray tomography allows minimally destructive 3D imaging over large volumes. Correlative combination of these techniques reveals fine detail of enamel rods, inter-rod substance, sheaths, crystallites and voids as a function of location. The degree of enamel demineralisation within the body of the lesion, near its front, and at the surface is visualized and quantified in 3D. We thus establish the paradigm of dental 3D nano-histology as an advanced platform for quantitative evaluation of caries-induced structural modification.

© 2022 The Authors. Published by Elsevier Ltd. This is an open access article under the CC BY license (<http://creativecommons.org/licenses/by/4.0/>).

\* Corresponding author.

E-mail addresses: [cyril.besnard@eng.ox.ac.uk](mailto:cyril.besnard@eng.ox.ac.uk) (C. Besnard), [ali.marie@eng.ox.ac.uk](mailto:ali.marie@eng.ox.ac.uk) (A. Marie), [petr.bucek@tescan.com](mailto:petr.bucek@tescan.com) (P. Buček), [sisini.sasidharan@eng.ox.ac.uk](mailto:sisini.sasidharan@eng.ox.ac.uk) (S. Sasidharan), [R.A.Harper@bham.ac.uk](mailto:R.A.Harper@bham.ac.uk) (R.A. Harper), [shashidhara.marathe@diamond.ac.uk](mailto:shashidhara.marathe@diamond.ac.uk) (S. Marathe), [kaz.wanelik@diamond.ac.uk](mailto:kaz.wanelik@diamond.ac.uk) (K. Wanelik), [G.Landini@bham.ac.uk](mailto:G.Landini@bham.ac.uk) (G. Landini), [R.M.Shelton@bham.ac.uk](mailto:R.M.Shelton@bham.ac.uk) (R.M. Shelton), [alexander.korsunsky@eng.ox.ac.uk](mailto:alexander.korsunsky@eng.ox.ac.uk) (A.M. Korsunsky).

## 1. Introduction

Dental caries remains a worldwide health problem affecting billions of individuals[1,2]. Despite numerous efforts to develop new preventive and therapeutic strategies, there is still no properly efficient treatment for caries. Understanding the demineralisation process taking place in dental caries at the micro and nano-scale is essential to shed light on the disease progression and potentially identify the means to arrest or reverse it.

Enamel is a dental tissue with a unique hierarchical structure, Fig. 1a. It is composed of hydroxyapatite (HAp) nanocrystallites, organised into rods  $\sim 5\ \mu\text{m}$  in diameter and an inter-rod substance  $\sim 2\ \mu\text{m}$  in thickness[3–5] with a ‘sheath’ surrounding the rods[6]. In enamel caries the tissue demineralises heterogeneously[7,8] resulting in four identifiable regions[9,10] visible histologically at relatively low resolutions (mm to  $\mu\text{m}$ ). These regions reflect the porosity changes occurring at the micro to nano-scales (across rods, inter-rods and crystallites)[11–14]. A description of etching patterns has been previously outlined to differentiate demineralisation (using acid solutions), namely type 1 and type 2 (preferential demineralisation in rods and inter-rod substance respectively)[15]. High-resolution transmission electron microscopy (TEM) analysis used in previous studies[16–18], provided an excellent illustration of the nature of HAp crystallite anisotropy in demineralised enamel. High-resolution analysis of human enamel is required to investigate the variations in dissolution rates between neighbouring crystallites which could arise from the intergranular amorphous calcium phosphate phase, high-angle grain boundaries, the presence of organic clusters[19–21], and defects[22].

Two of the common techniques used to examine enamel are light microscopy and radiography[23,24]. Darling in the 1950s [23,25] summarised that four zones can be observed in early carious enamel based on the variation of birefringence in enamel, referred to as: surface zone, body of the lesion, dark zone and translucent zone. The observation of these zones using light microscopy is due to the variation of refractive index of enamel and the size of the molecules of the media used to immerse the sample (air without media)[26,27]. Quantification of porosities in the carious enamel has been undertaken in different zones[28–30,25]. However, it has been reported that the translucent zone could not always be identified and also that depending on the immersion medium used to study the optical response, both dark and translucent zones could be difficult to identify[25,30].

It is important to consider that in the past analysis of images based on birefringence, each image averages the information over the whole thickness of the sample. This resulted in values of porosity percentages measured without detailed knowledge of the internal structure. Consequently, the shortcomings of the analysis to date are the narrow fields of view and the limitation of 2D images with missing detail of structure across the thickness of the sample. There is therefore a need for multiscale comprehensive analysis that include a spatially resolved sub-surface visualisation in 3D. Using a light microscopy image as reference, we propose the use of focused ion beam and scanning electron microscopy (FIB and SEM) and X-ray tomographic mapping of the carious lesion is as the techniques for three-dimensional (3D) nano-characterisation.

Focused ion beam (FIB)[31] in combination with scanning electron microscopy (SEM)[32] (referred to as ‘FIB-SEM’), is a powerful material nano-machining analytical technique[33–36]. It combines the advantage of high accuracy milling and visualisation at sub-micron scales (FIB and SEM) and can be used for preparing micro-volume samples (e.g., lamella) for further imaging, quantitative analysis or mechanical analysis of materials. This has been used to study enamel with and without modifications (carious, artificially demineralised)[4,13], and dentine[37]. Although FIB-SEM

does not offer sub-nanometre imaging resolution compared with TEM, it has the advantage of allowing localised 2D and 3D reconstruction at larger scales, which is valuable for different types of spatial analysis whilst maintaining sub-micron resolution. [Supplementary information](#) (SI) Note 1 and SI-Table S1 review detailed the FIB-SEM applications to dental research and summarised the work in two dimensions (2D) and 3D FIB-SEM processing of dental tissues. For the state-of-the-art and recent applications of 3D imaging analysis with the comparisons of resolution and dimension of areas of interest achieved, see[13].

It has been well established that different degrees of demineralisation occur within a carious lesion, as reflected in the zones traditionally identified using light microscopy. However, to the best of our knowledge, there has been no systematic characterisation studies of carious enamel utilising high-resolution FIB-SEM 2D and 3D imaging with quantitative micro- to nano-structure analyses. In the current study, the enamel was studied over larger areas using state-of-the-art correlative techniques to provide new insights into enamel caries structure in correlation with the optical zones described more than seven decades ago[23,38]. It is remarkable to note that in all this time it has not been identified how the underlying nanostructure leads to the distinct appearance of specific carious lesion zones. The present work aims to enrich the knowledge of ultrastructural differences within the carious lesion with reliable quantitative information, and is not directly targeting clinical practice although the new insights can inform the methods that can be used in existing and developing therapeutic approaches. FIB-SEM was used in combination with synchrotron X-ray tomography to visualise the ultra-structural changes in enamel caries at different scales, Fig. 1a. Different locations within the carious lesions were studied and compared with normal enamel using digital analysis tools. Numerous individual locations were selected from a light microscopy image and were used for correlative analysis, Fig. 1.

## 2. Results – Discussion

### 2.1. Analysis of the cross-sections – Imaging and statistical analysis

The feasibility of using FIB-SEM to image subsurface structures and compare structures from different zones in the enamel caries that has been previously explored, has been used to screen the sample in the current study. In this section, the ultra-structural changes in enamel resulting from dental caries were analysed at several locations of the sample assigned to zones based on the light microscopy image, Fig. 1b and SI-Fig. S1a (more details in the Methods section).

The cross-sectional SEM images revealed differences in the structure even after the initial rough milling as visualised in SI-Fig. S2. Further SEM analysis after thinning disclosed more porosities in the enamel at Location (abbreviated Loc) 9, 8 than in the normal enamel from the region adjacent to the lesion and close to body of the lesion (e.g., Loc 23), Fig. 2. These changes appeared to coincide with the light microscopy image and the corresponding tomographic reconstruction in SI-Fig. S1a,b. Fig. 2 shows high-resolution SEM images of enamel from different locations after thinning with details of variations in the structure observed (additional locations are shown in SI-Figs. S3–6, corresponding secondary electron image (SEi) of low magnification images in SI-Figs. S7,8, and further structural imaging details in SI-Figs. S9–12). The typical enamel rod and inter-rod material arrangement was clearly observed in many locations (except the locations in the non-carious region), together with shape dissimilarities between different rods which can be analysed due to the demineralisation of the structure, see SI-Fig. S13.

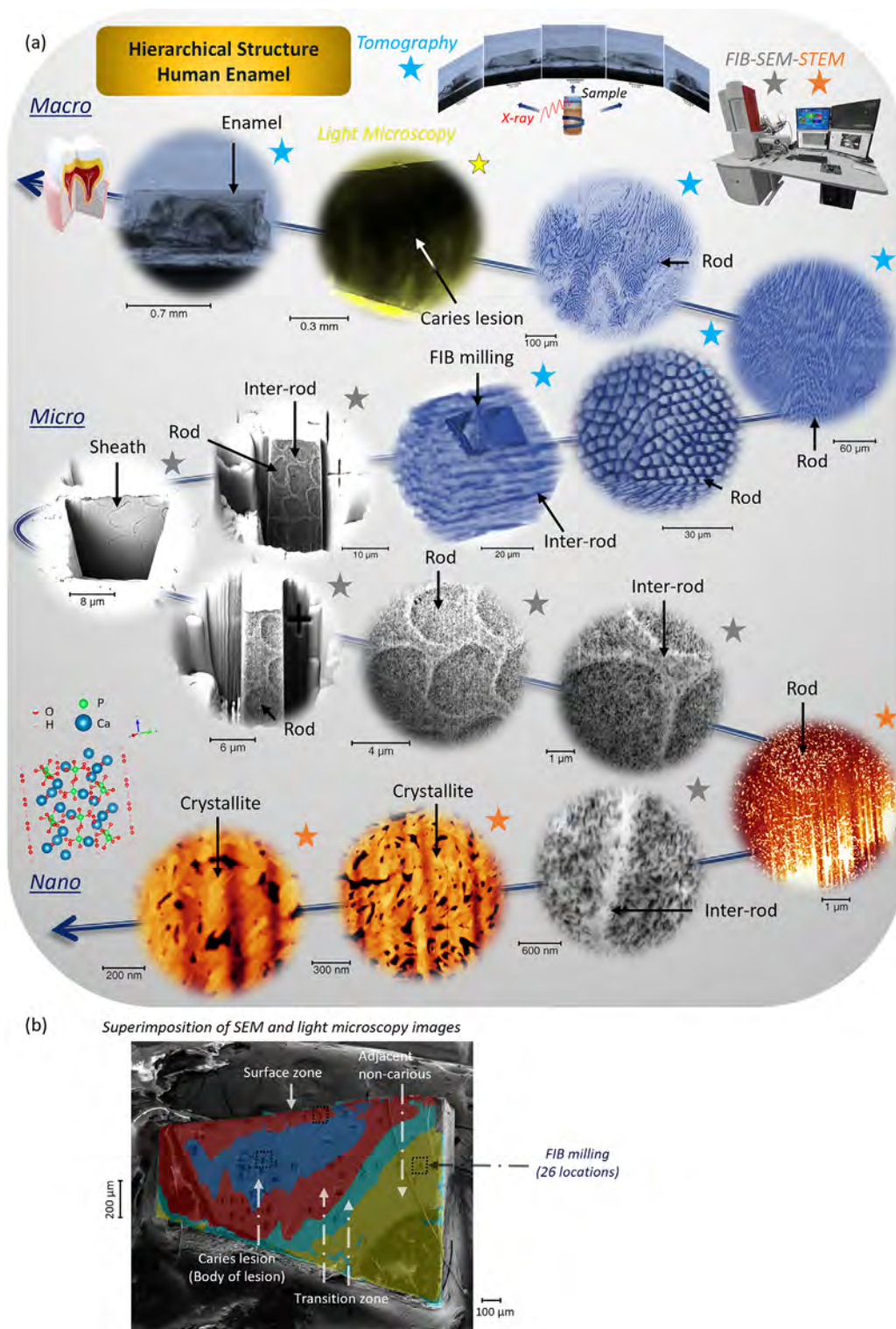


**Fig. 1.** Ultrastructural analysis of human enamel caries using light, electron microscopy and X-ray imaging. (a) Hierarchical structure of enamel illustrated using several imaging techniques highlighted with coloured coded stars according to techniques (blue, yellow, grey and orange), X-ray synchrotron tomography (projection and 3D images, blue), light microscopy (yellow), FIB-SEM (grey), and scanning transmission electron microscopy (STEM) in SEM (orange), with some 2D and 3D images. This succession of images highlights the organisation of enamel into rods and inter-rod substance, the complex arrangement of rods, and crystallites, to the crystal structure of hydroxyapatite. In the inset, projections from X-ray tomography acquisition, and FIB-SEM Tescan Lyra 3. (b) SEM image superimposed on a light microscopy image with the description of the zones in carious enamel, and the locations (total number 26 for cross-sections; see Fig. 4 with cross-sections and slice and view, and the Methods section for the details of the determination of the zones and the assigned colours) used to characterise the sample (the boxes show a few FIB-SEM regions). In the figure, the 3D renderings of tomography were processed as well as the slice and view data, further details are presented in the Methods section of this study. The crystal structure was rendered with VESTA[39] from CIF file 203027 Inorganic Crystal Structure Database (ICSD)[40,41]. The optical image was modified from[13] with the permission of Elsevier and Copyright Clearance Center. (For interpretation of the references to colour in this figure legend, the reader is referred to the web version of this article.)



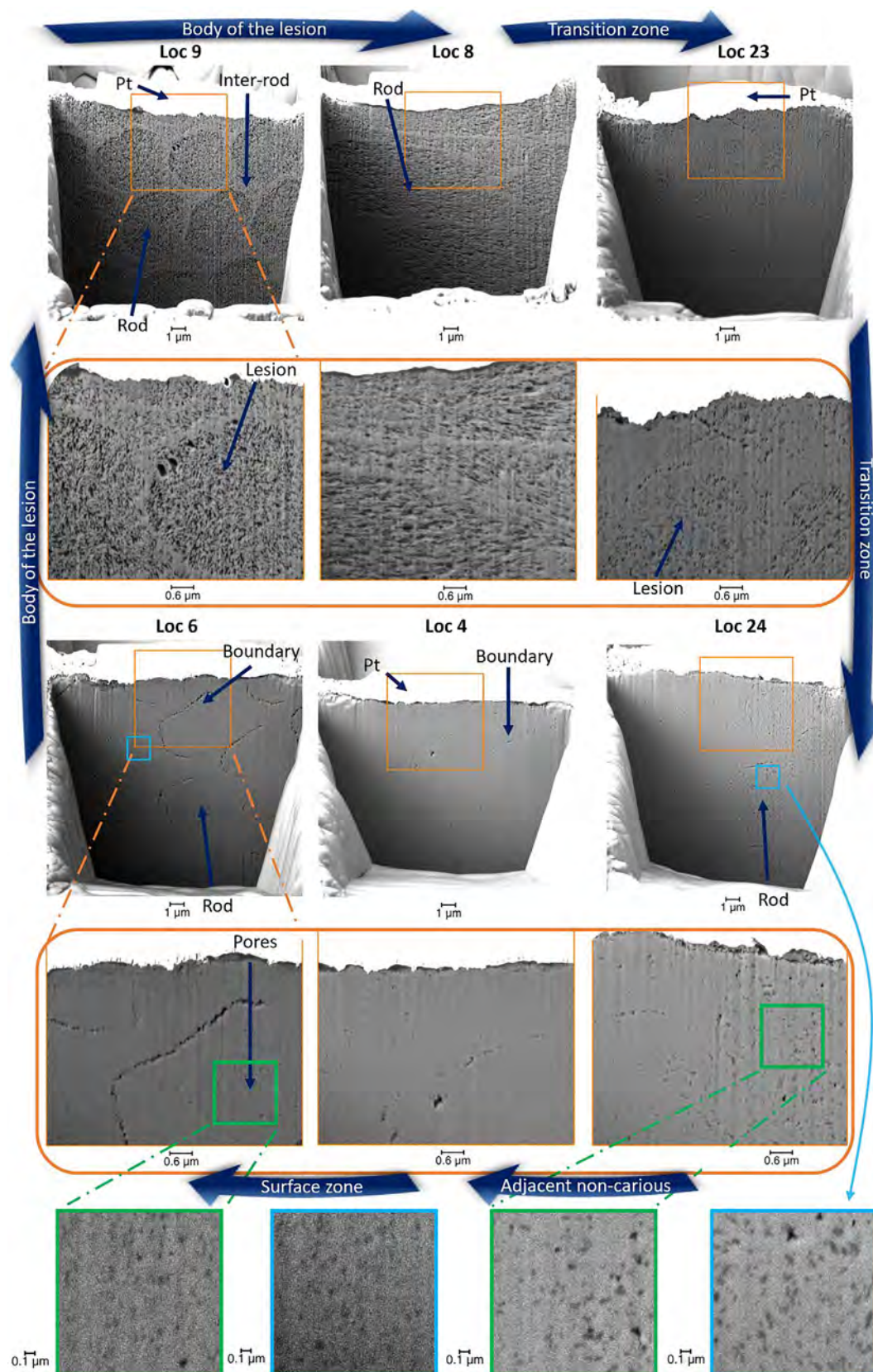


**Fig. 2.** 2D SEM imaging and structural characterisation of various locations in the carious sample at different magnifications. Backscattered electron image (BSi) of different locations in the sample in the different zones previously defined (following the light microscopy image analysis), e.g., adjacent to the carious region considered normal enamel (Loc 4) and close to the surface (Loc 6), with higher magnification of each location highlighted (orange box), and two more zoom images for Loc 16 and Loc 4. Additional locations and images are detailed in SI-Figs. S3–12. The spatial coordinates of the locations in relation to the carious lesion are depicted in Fig. 1b and SI-Fig. S1a. Clear differences in the structure were visualised. This method led to distinction of features in the enamel at high-resolution using a systematic process. The ‘boundary’ noted on the figure was also analysed and discussed in this study. Further details on the zones are provided in the Methods section. (For interpretation of the references to colour in this figure legend, the reader is referred to the web version of this article.)

Inhomogeneity of porosity was identified at different locations. For instance, in the carious lesion (Loc 8, 9, 12, 13) demineralisation of the enamel rods was visually more evident than the inter-rod space (Fig. 2 and SI-Figs. S3,7,9). In contrast, Loc 23 and Loc 24, (close to the border of the caries) had less obvious porosities in comparison with Loc 9, although was more porous than the non-carious region (normal enamel Loc 4). Higher magnification images of the cross-sections are detailed shown in Fig. 2 and revealed more details of enamel dissolution and HAp crystallites, with removal of enamel material (additional images in SI-Figs. S3–6,9–12). From the observed structure, it could be observed that there was a different degree of damage of the structure. In Loc 13, the pores are seen with evident degradation of the structure and these were visualised in other locations in the body of lesion too. However, in the surface, and transition zone, porosity was also seen but with less obvious hole features as highlighted for Loc 6 and Loc 24 in Fig. 2. The variation in porosity agreed with the region of the lesion observed in the light microscopy image and tomography data (Fig. 1 and SI-Fig. S1a–d).

At the micro-scale, demineralisation patterns were previously reported to indicate the preferential loss of mineral [42]. It is suggested etching pattern type 1 and type 3 enamel demineralisation in the carious region, whereas type 1 was evident for the Loc 23. Greater magnification showed there was variation of dissolution of enamel within rods and inter-rods themselves. The structural modification of the enamel can be combined with diffraction data and provide additional details including phase, lattice information [4]. Additionally, an indication of amorphisation was suggested within the carious region based on diffraction results [43] which could then be compared with other locations.

## 2.2. Analysis of cross-sections – Loc 6 close to enamel surface

In the region close to the enamel surface (Loc 6 and Loc 5, 7), the 2D imaging analysis revealed a thin trench-like boundary delineating an enamel rod (Fig. 2 and SI-Figs. S6,7) which was preferentially localised in the inter-rod of the enamel suggesting it was the sheath around the rod. The sheath in the inter-rod could also be demineralised, similar to the early stages of enamel caries where it has been reported that inter-rod was preferentially demineralised as shown by TEM [11] and in the advancing front of caries from backscattered electron imaging [12] and with synchrotron tomography [13]. The quantification of the dimension of the boundary showed a Euclidean distance around 50 nm that varied along the rods, Fig. 3a. Furthermore, the sheath boundary was discontinuous and became thinner towards the tail of the rods, as shown in Fig. 3b, with the distance computed from the region outside the segmented sheath. This showed the non-sheath region, and the distribution of this region with the connected area. It has been reported that inter-rod enamel contains more organic material compared with rod enamel [44,45], organic-rich regions which are suggested to remain from enamel development [45]. Additional details on this region are detailed in [Supplementary information Note 2](#).

The previous analysis, suggested that the boundary corresponded with the enamel sheath (also termed 'gaine' [18]). Further observation of the region closer to outer enamel surface visually revealed less demineralisation in term of pore distribution in comparison with other locations in the sample, e.g., Loc 9. This finding has previously been reported using various techniques, which are in agreement with the current SEM findings (Fig. 2). This region is often referred to be the 'surface zone' as opposed to the 'body of the lesion', where the main loss of mineral occurs [8]. Further details on the analysis of enamel and surface zone are reported in [Supplementary information Note 3](#).

Additional to the evident boundary, some demineralised areas within the enamel rod and inter-rod structure were identified, see Figs. 2 and 3. Less demineralisation was seen on the top portion of a rod in comparison with its core as illustrated in Fig. 3c, Loc 6 obtained by computation of the distance from the region outside the sheath and porosity. The distance was larger with  $\sim 1 \mu\text{m}$  on top of the rod and inter-rod in comparison with  $\sim 0 \text{ nm}$  in the core. Loc 6, Fig. 3, shows that the distribution of porosity followed a pattern around the sheath which could give details in the pathway of the demineralisation. The distance analysis was also carried out on locations from carious regions which revealed larger distances between inter-rods in comparison with rods, for Loc 9 going from  $\sim 200 \text{ nm}$  to  $\sim 0 \text{ nm}$ . Interestingly, the inter-rod could be divided into three distinct regions in the base of the rod ('tail'), with two borders of the rod, and a central region that presented with more porosity. In comparison with Loc 6, one location close to the surface enamel could correspond with the sheath location. In Loc 2, adjacent non-carious region (normal enamel), the distance was higher in comparison with the carious region, as the area presented less porosity. In the regions between body of the lesion and non-carious enamel, the maximum distance was found to be larger than within the body of the lesion Loc 9, and interestingly Loc 16 showed important contrast in the demineralisation from the rods observed. In Loc 22, the inter-rod was identified with less demineralisation than the rods. Further analysis in a few locations were carried out at higher resolution and smaller regions are reported in SI-Fig. S14a.

As the analysis used static rather than dynamic imaging, it was difficult to confirm whether all the pores in the boundary resulted from the FIB thinning process, or were due to the demineralisation in the lesion. However, in comparison with the structure of normal enamel [4,13,46], locations from close to the surface enamel and adjacent to the carious lesion, it is suggested that the thinning process might have led to the formation of some pores in the softer material, e.g., sheath. Nevertheless, differences in enamel characteristics were very evident in the lesion compared with normal enamel, which clearly showed the difference in the structure due to the effect of caries demineralisation thus allowing for quantitative comparisons.

Area measurement of the porosity observed after FIB-SEM analysis was carried out in several locations to ensure examination of a region located more in the rods than inter-rods, as summarised in Fig. 4. Locations were assigned according to the zones, surface zone, non-carious, body of the lesion, and the transition zone based on the light microscopy image. Systematic analysis was done to compare regions of interest. The difference between the average porosity in each zone is significant based on One-way ANOVA analysis (the surface zone is  $8.13 \pm 3.14\%$ ; the body of the lesion, which is the highest value, is  $40.64 \pm 2.21\%$ ; the transition zone is  $19.02 \pm 9.13\%$ ; the non-carious region, which is the lowest value, is  $0.64 \pm 0.47\%$ ). The lowest porosity in the transition zone was found in locations close to the non-carious region, but as seen on the BSi images, there was some variation within the same cross-sections, shown by the highest standard deviation. Higher values were found here in comparison with previous values of porosity reported in the zones, however, it needs to be considered that in the body of lesion for instance, the rods were generally more demineralised than inter-rods, resulting in an overall lower porosity. In addition to local porosity analysis, specific analysis of the porosity in rod and inter-rods were measured and differences were found with a higher area measured in the rods (SI-Fig. S14b). Multiple localised regions of interest were manually selected for the area comparisons as shown in SI-Fig. S14b, Region 1 and Region 2. The area of porosities of the whole region was measured as  $\sim 23\%$  of the total area, which was similar to the volume of porosities reported in the literature [47]. However, these are 2D values for area from cross-sections.



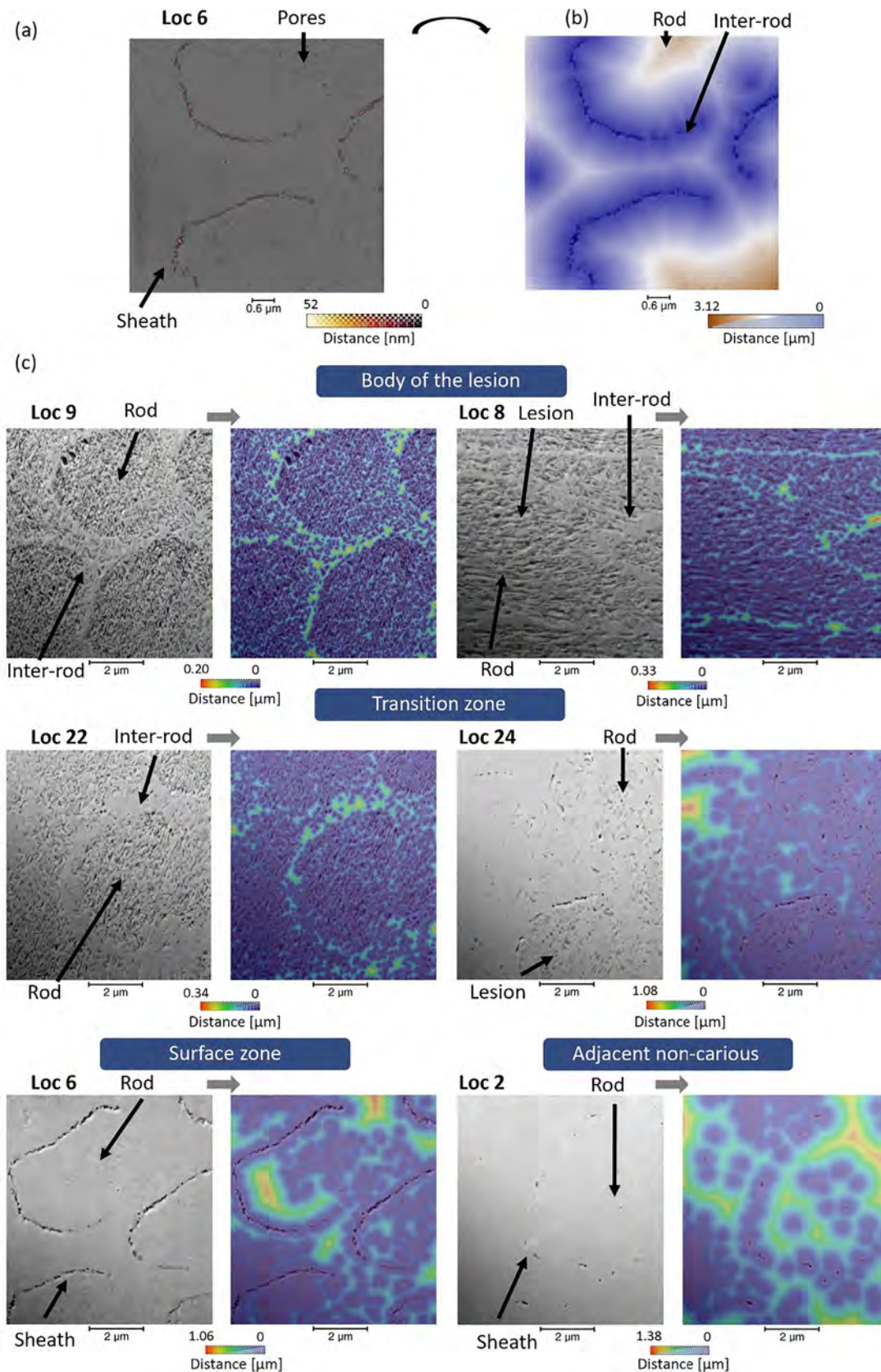


**Fig. 3.** Sheath analysis of the Loc 6 and the Euclidean distance analysis of the regions around porosity of several locations in the sample. (a) Analysis of the dimension of the sheath in Loc 6 after filtering (fast Fourier transform (FFT), AI filtering, shading correction) and segmentation. (b) Distance analysis of the region outside the sheath (related to the region analysed in (a)) superimposed with filtered BSi. (c) BSi cross-sections of Loc 2, 6, 8, 9, 22, and 24 after AI filtering to cover the different zones. Illustration of the computation of distance performed on segmented regions (similar to the invert of the porosity regions) superimposed with the BSi following methods detailed in SI-Fig. S15. This illustrated preferential remaining regions resulted from the carious process.

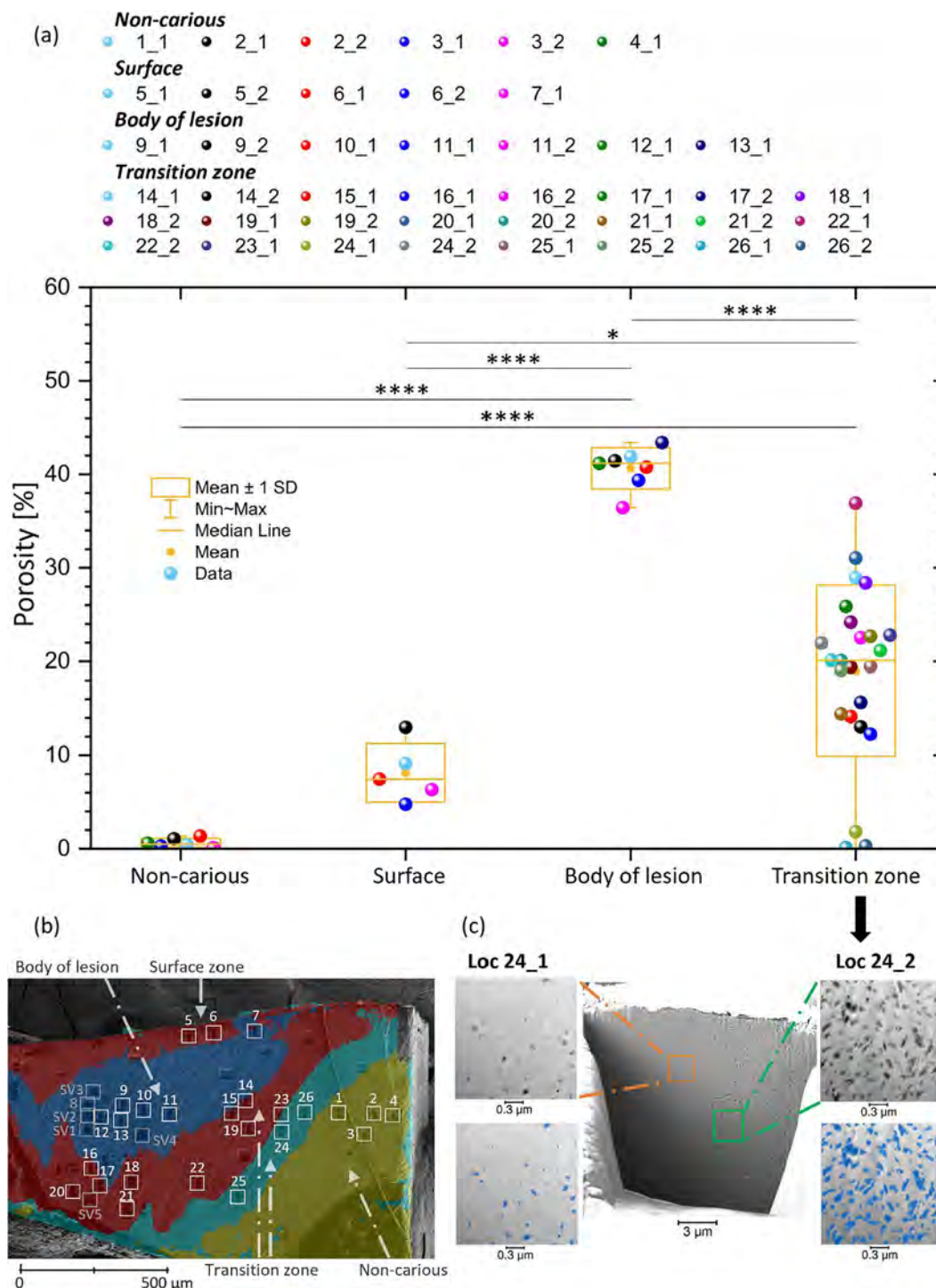


**Fig. 4.** Porosity measurement analysis of the FIB-SEM thinning Loc 1 to 26 covering the various zones in the carious enamel. (a) Plot of the porosity (being the ratio of the Area of the segmented region over the total area of the corresponding SEM region of interest (ROI)  $A_{ROI} = A_{segmented}/A_{ROI}$ ) from the analysed locations in the different zones of the sample (the determination of the zones is detailed in the Methods section). One-way ANOVA test with post hoc Tukey's test was carried out. \* represents  $p < 0.05$  and \*\*\*\* represents  $p \leq 0.0001$ . (b) Image of the superimposition of the SEM and light microscopy image for direct identification of the zones, mentioned in Fig. 1b, and of all the locations of this study (note Loc 8, referred to as the longitudinal was not analysed and detailed in this figure, due to large differences in orientation compared with the other locations, as well as 'SV' referred to as the slice and view locations being obtained with a different process). (c) The illustration of the analysis of the density with an example for Loc 24 with two rods analysed referred to as 24\_1 and 24\_2 (same numbering was kept for other location). BSI after AI with and without the segmented dataset and the low magnification of the BSI. Each location is detailed in SI-Figs. S16-19.

In the inter-rod region, a border with less porosity was clearly visible in Loc 9, which corresponded with the rod sheath, SI-Fig. S14c. The computed distance of the border up to 124 nm, was larger than the sheath distance measured in the Loc 6 close to surface enamel, 52 nm. These findings were in agreement with

similar reported comparisons between AFM and TEM mentioned previously (see [Supplementary information](#) Note 3). This supported the possibility that the boundary was more resistant to acid dissolution as compared with rods in the carious region, despite the presence of several undissolved locations in rods.



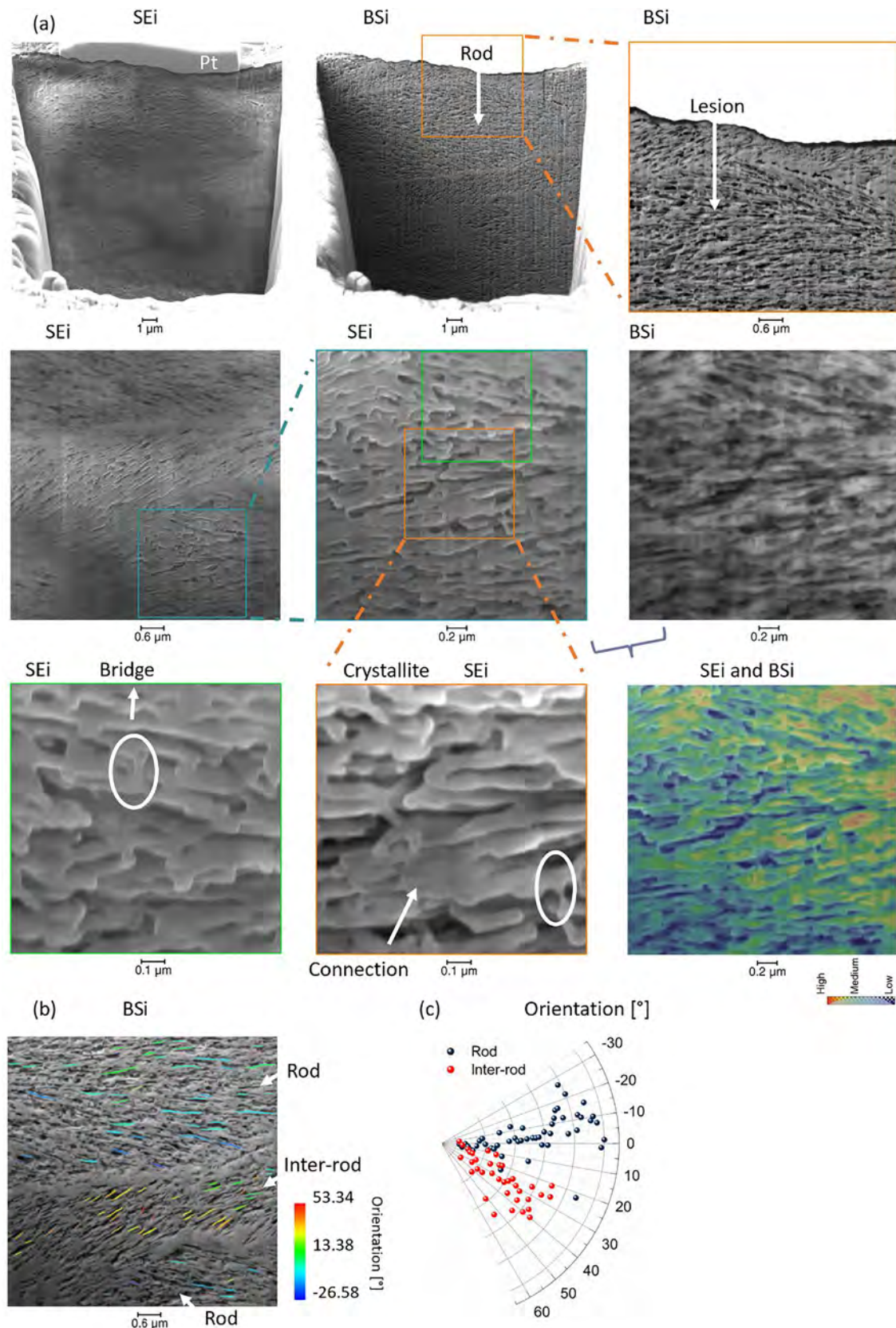


**Fig. 5.** Characterisation of Loc 8 with SEM and the observation of the demineralisation from another rod orientation. (a) SEM analysis of different locations highlighting the enamel lesion, anisotropy and differences between rod and inter-rod substance. The magnified region highlights the presence of bridges (additional details, SI-Fig. S22). Contrast obtained from the superimposition of BSi and SEi images (after AI and Gaussian filtering respectively). A colour map was applied to BSi (greyscale variation) and greyscale for SEi. (c) Analysis of the orientation of the structure in rods and inter-rod, details of the structure are shown in SI-Fig. S21.



Elemental analysis of locations in the sample was carried out with energy-dispersive X-ray spectroscopy (EDS) to extract chemical content and is summarised in SI-Fig. S20 for SEM analysis. Ca and P were detected as expected from HAP (ideal form  $\text{Ca}_{10}(\text{PO}_4)_6(\text{OH})_2$  [48]), Ca (emission line  $K_{\alpha 1} = 3691.68$  eV) and P ( $K_{\alpha 1} = 2013.7$  eV) [49], as well as an intense peak for Au and Pd resulting from the sputter coating. It has been reported that fluorine (F) and magnesium could be found in enamel structure [19,21,50], these were not significantly detected, this could be due to the limitation of the sensitivity of the EDS methods or due to the sample itself. A line scan was carried out going from the non-carious region to the surface of the enamel and showed no major modification of the composition, SI-Fig. S18b.

### 2.3. Analysis of Loc 8 – Longitudinal orientation

To visualise the crystallite orientations and the network of porosities along the rods, Loc 8 was further analysed, Figure 5 and SI-Figs. S21,22. Morphologically both rods and inter-rod showed evident demineralisation. Crystallites exhibited clear anisotropy in the pattern of demineralisation (gaps between crystallites with interrupted areas tightly packed as seen in perpendicular cross sections). Similar observations have been reported earlier on bovine enamel [51] where some locations between neighbouring crystallites might not be separated by a sheath but were in close contact. In Figure 5a, small connections between enamel structures were identified and referred to as 'bridges'. Volume was considered as a limitation in this cross-sectional analysis. Due to the limitation of the compositional analysis achievable in SEM from thick regions, the chemical composition of these bridges could not be determined, however, these could have contained minerals with significant different orientations or organic substance, or mineral salts which have previously mentioned [52]. These bridges were about 20–35 nm in diameter and almost double in length (summarised in SI-Fig. S7b).

Image analysis along the rods facilitated visualisation and characterisation of HAP crystallite orientation (the trajectory of the crystallites), as summarised in Figure 5b. The pathway (orientation) of the crystallites was identified visually and angular measurements were calculated in both rod and inter-rods. The data suggested that the orientation of the crystallites was not homogeneous, as widely reported in the literature [44,53–58]. However, it was evident that HAP crystallites followed a trend in the trajectory, but there were also some variations with the neighbouring structure.

In the Loc 8, additional analysis was carried out on the acquired SEi and BSi. It is well reported that secondary electrons and backscattered signals have different origins on the observed sample, hence extra analysis can be performed by superimposition of the SEi and BSi images acquired from the relevant detectors to gather additional details [59]. It was interesting to observe contrast differences using BSi and the difference was seen after the superimposition of the SEi revealing a higher contrast region, as shown in Loc 8 in Fig. 5a. Such analysis is useful as it has been reported that image analysis of bone has shown a correlation between the grey value of backscattered electron imaging and the corresponding density of the bone [60,61].

The combination of two beams in FIB-SEM enabled high-resolution imaging and analysis at micro and nano scales to reveal subsurface ultra-structural details of enamel, including rod, inter-rod, sheath and crystallites without performing TEM. This technique can be used to characterise the demineralisation and/or remineralisation effect on surface/sub-surface enamel. Although the resolution allows visualisation of individual crystallites, their trajectory (orientation) and provides quantitative analysis of the porosity distribution in the sample, there are limitations as it is

not possible to acquire lattice details of HAP and nano structure, e.g., the so called central dark line [21,62–64]. This nanostructure is usually identifiable using TEM and allows observation of changes in the HAP lattice. Crystallites were previously analysed in carious lesions using TEM revealing a complex structure, where a central region of the crystallite was visualised and reported as a 'perforation' of the crystal, as well as demineralisation at the periphery of the crystallites, but also remineralised crystal [11,14,17,65–69]. Further ultra-analysis can be achieved using TEM in combination with atom probe tomography and other techniques, such as chemical analysis. These nano-analyses revealed potential locations where the enamel crystallite demineralisation started as a central dark line, grain boundary with large angle, organic region, and difference in chemical composition [20,21] which cannot be revealed by SEM observation.

The overall 2D cross-section analysis showed that the enamel porosities due to demineralisation were observed with connected and/or isolated demineralised regions, and this was extended with 3D characterisation.

### 2.4. 3D analysis – FIB-SEM slice and view

Slice and view analysis of Loc SV1 was carried out to obtain a 3D view of the evolution of the lesion along the direction of the slicing. This revealed hidden porosities and a pathway of the lesion (Figure 6 and SI-Fig. S23). In the region of interest, rods and inter-rods were selected (structure suggested from the demineralisation) and visualised, following the alignment and denoising of the dataset and the stack of slices was reconstructed and analysed. The thickness of the slices was  $\sim 8$  nm on SV1. Extracted slices from the stack clearly showed the degradation (dissolution) of the enamel according to the depth of carious lesion, this pattern was not restricted to one slice as seen in the cross-sectional analysis, Figure 6. Nano porosities across the total milled volume appeared with dark greyscale values, and the interconnectivity of pores followed a complex organisation. The nano-network of porosities provided a possible explanation for the reported difficulties in remineralising deep enamel carious lesions. This network could further enhance the flow of acids deeper in the lesion, allowing a preferential pathway across the network of voids. In contrast, normal enamel (additional details see our previous studies [4,13]), typically presented with a noticeable sheath boundary, in agreement with Cougot *et al.* [46]. The inter-rod in Loc SV1 had a scarcity of pores. Additional details on slice and view and 3D analysis can be seen in SI-Figs. S24–28 for the Loc SV2 (SI-Movie S1, available on Mendeley Data [70]), SV3, SV4 and SV5 with a lower voxel size. Anisotropy of the demineralisation with preferential demineralised regions was also observed in the slice and view and at the end of the slicing, SI-Fig. S29.

### 2.5. Correlative analysis – X-ray synchrotron tomography and FIB-SEM and light microscopy

A correlation of the resolution and dimension of the images acquired and reconstructed with FIB-SEM analysis and synchrotron X-ray tomography datasets was carried out to analyse enamel at different scales to reveal localised alterations in its structure (Fig. 7 and SI-Figs. S24,25,30, SI-Movie S2, movie available on Mendeley Data [70]). The milled cross-sections with and without undercut milling, and all milled slice and view locations were imaged using both imaging modalities. In the synchrotron tomography data (resolution of  $0.325 \mu\text{m}$ ), Pt locations (deposited during FIB process) were detected on the tomogram and the locations of the cross sections, STEM and slice and view regions were extracted. The information obtained from synchrotron dataset with lower greyscale values, is shown here with more details. This was

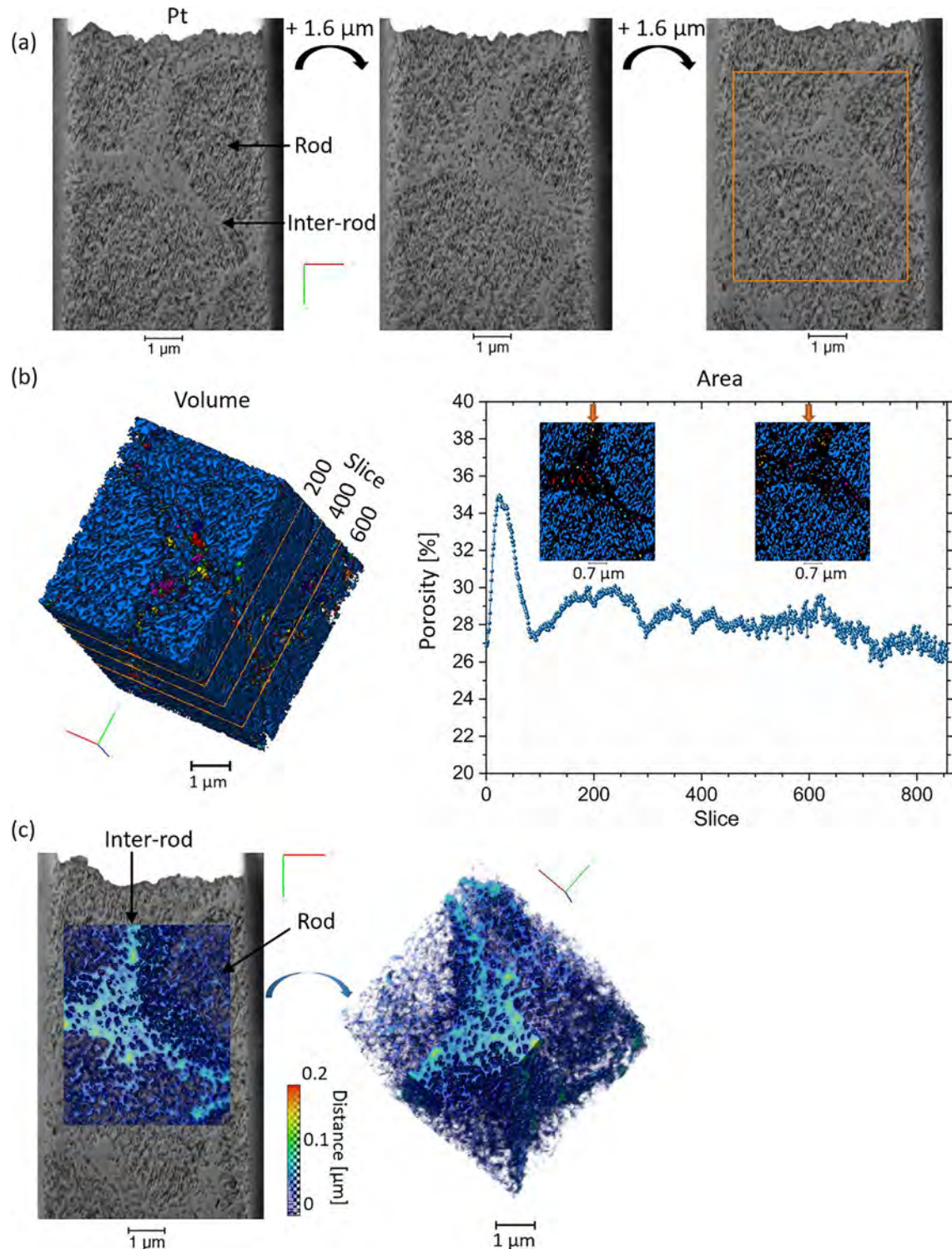


**Fig. 6.** 3D FIB-SEM slice and view analysis of the Location SV1 with 2D and 3D computation. (a) Sequence of virtual slices of the BSi after FFT filtering, alignment, reduction of size, AI filtering and extraction of ROI, spacing of 1.6  $\mu\text{m}$  (dimension  $\sim 6.22 \times 11.92 \times 6.85 \mu\text{m}$ ,  $779 \times 1491 \times 857$  pixels, voxel size 8 nm). (b) 3D rendering of the segmentation and 3D analysis of the pores with the colourmap assigned to each individual 3D region, plot of the porosity as a function of slices (being the ratio of the Area of the segmented region over the total area of the corresponding slice  $A_{\text{slice}}, A_{\text{segmented}}/A_{\text{slice}}$ ), and illustration of two slices extracted from the stack. (c) Volume rendering of the Euclidean distance of the spacing region with and without the slice from (a), and volume rendering of the thickness of the same slice from (a) with the superimposition of the Euclidean distance of the spacing region (dimension  $\sim 4.58 \times 5.50 \times 6.85 \mu\text{m}$ ,  $573 \times 688 \times 857$  pixels). Additional details for SV1 are shown in SI-Fig. S23. Reduction of the dimension in each axis of the stack was done to focus on the region of interest. A reduction in the dimension of slicing direction was also undertaken if necessary, to remove the first slices. Some of the first slices were excluded as they could also be covered with redeposition from the FIB machining. In some locations the probe current used to machine the volume prior to slicing was higher than the probe current used for slicing and the first slice of the acquired region was placed anterior to the front margin to retain the region of interest.



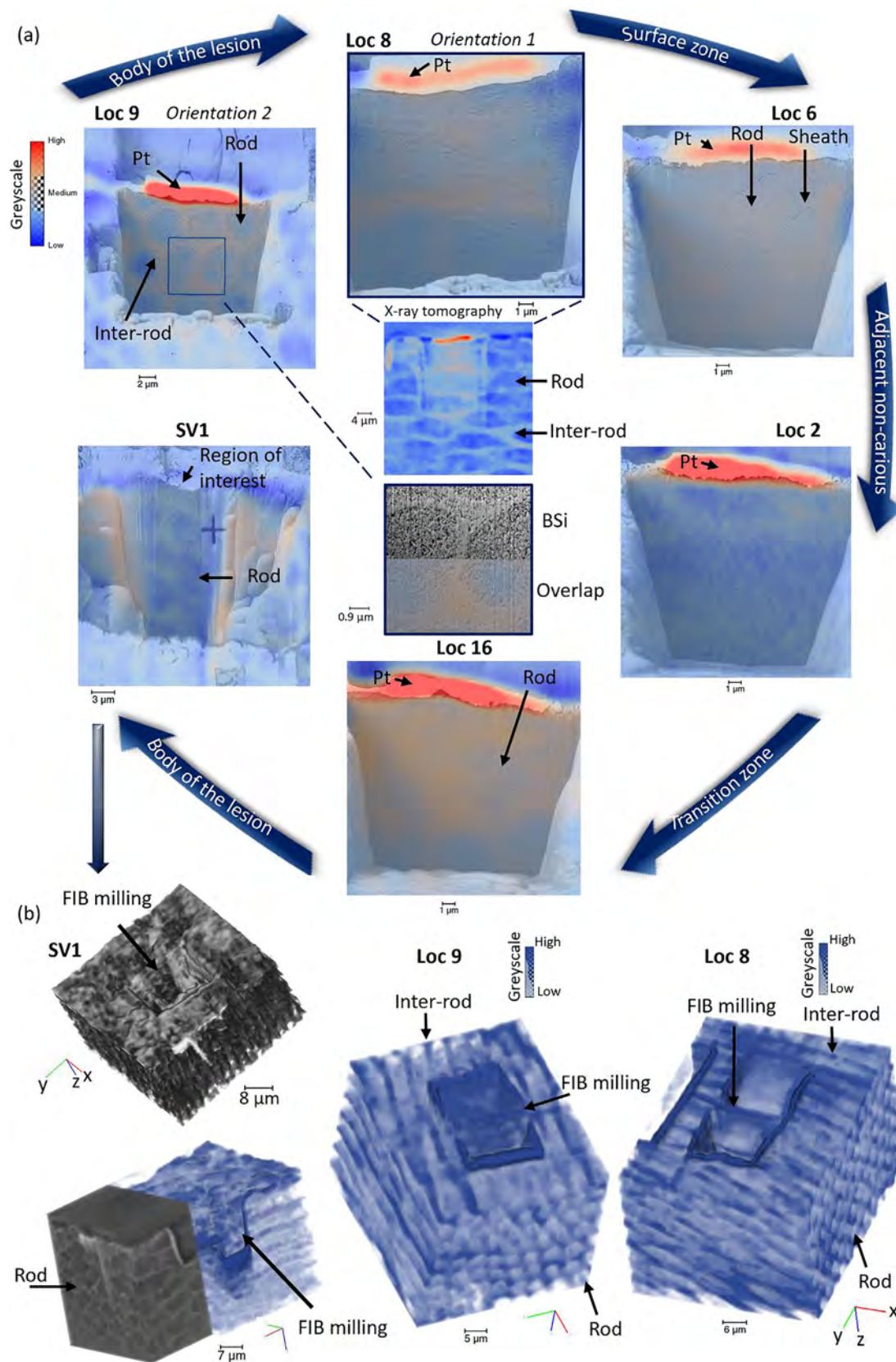


**Fig. 7.** Correlative imaging analysis of synchrotron X-ray tomography using 10x objective lens and FIB-SEM analysis. (a) Correlation of the tomography and FIB-SEM images (BSi) of five cross-sections (Loc 16 and 2 tomography acquired before the final thinning) to cover the various regions, and one slice and view after the thinning (tomography data 3D median filter). The images showed the superimposition of the X-ray tomography virtual slice with the BSi image of the cross-sections proving novel combination of tomography and FIB-SEM on enamel with the identification of the modification of the structure from the two imaging modes. An additional large dimension of the Loc 8 highlighting the rod paths in comparison with Loc 9 is shown (referred to as orientation 1 and 2). Additional details for Loc 9 are shown in SI-Movie S2 (movie available on Mendeley Data[70]) and zoom-in image in (a). (b) 3D rendering of SV1 after the slice and view, of Loc 9 and Loc 8 highlighting the location of the slicing and the structure of the rods in 3D (3D median filter). Additional details on the correlative analysis are shown in SI-Figs. S24b,25b,30, and for the 3D rendering of synchrotron tomography data SI-Figs. S31-39 covering several locations. Addition details illustrated in SI-Movie S3 available on Mendeley Data[70].

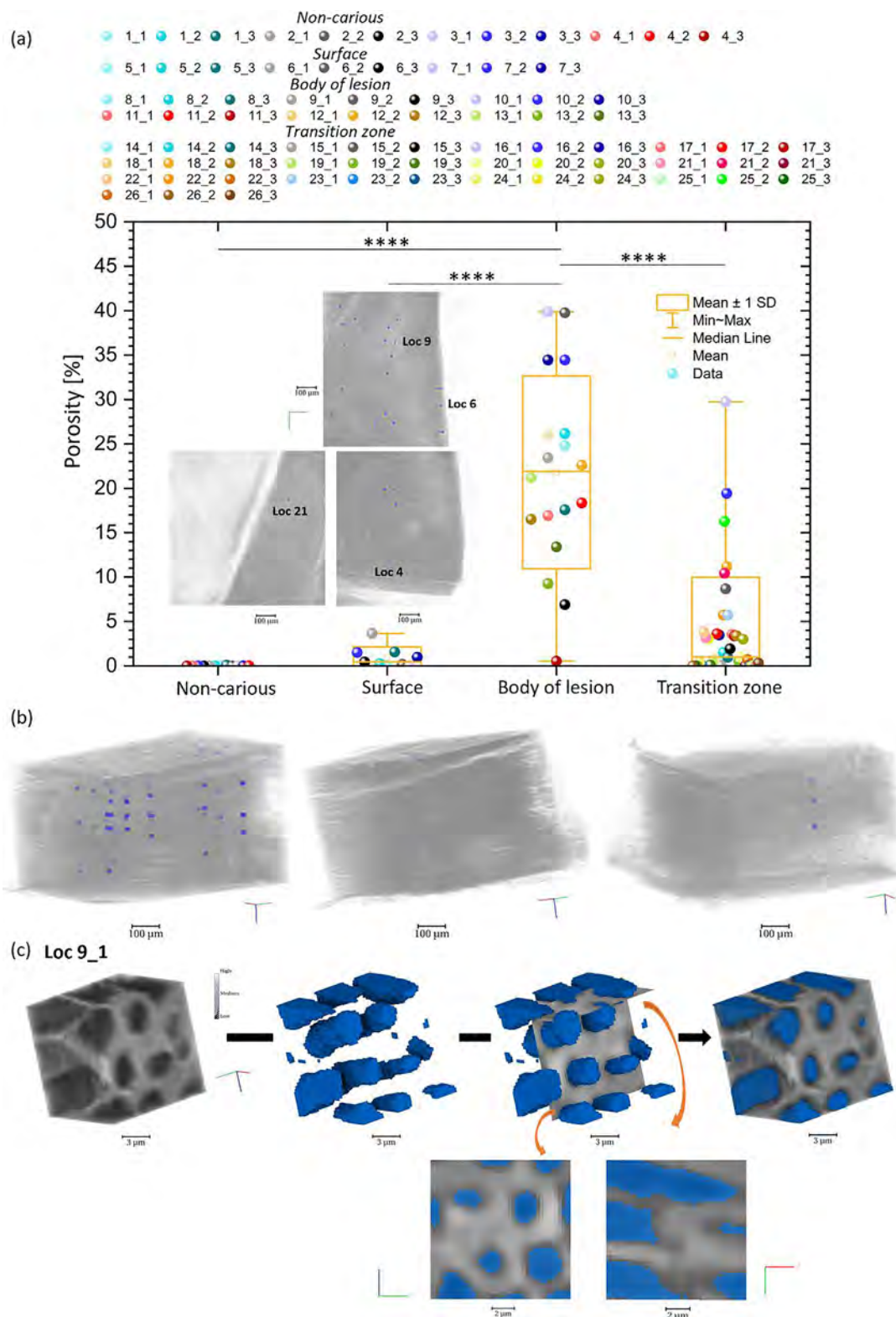


**Fig. 8.** Localised demineralisation analysis in 3D using synchrotron tomography data. (a) Plot of the ratio of the volume of the segmented data (corresponding with low greyscale) in each subregion (dimension  $12.675 \times 12.675 \times 12.675 \mu\text{m}$ ,  $40 \times 40 \times 40$  pixels) with inset the volume rendering of tomography data (3D median filter) of the enamel from three tomograms (dimension of each volume  $815.425 \times 815.425 \times 587.925 \mu\text{m}$ ,  $2510 \times 2510 \times 1810$  pixels, voxel size  $0.325 \mu\text{m}$ ) and the details of various region of interest analysed, in several locations and assigned to the zones based on the light microscopy image. This corresponds to the analogy with the 2D analysis, the porosity being in that case the ratio of the volume of the segmented region over the total volume of the corresponding region. One-way ANOVA test with post hoc Tukey's test was carried out. \*\*\*\* represents  $p \leq 0.0001$ . Three regions at different depth per location referred to as \_1, \_2 and \_3. (b) Volume rendering of the three datasets and superimposition of the locations analysed. (c) Details of one subregion, Loc 9\_1 with the 3D rendering (3D median filter) before and after segmentation of the low grey value corresponding with the degraded structure. Superimposition of the segmented region and extraction of two virtual slices in xy and yz, rod structure was visualised. Addition details in SI-Figs. S40,41.



demonstrated with a superimposition of BSi and slices from the reconstructed tomography data in similar locations, Fig. 7a. There was an enhanced porosity distinction in the rod and inter-rod regions, which was only noticed with greyscale modification along the rod cross-section without high-resolution structure details[13]. In the carious region, the shape of inter-rods and rods were clearly visualised also with the distinction of the rods' orientation from the Loc 9 and Loc 8, and in the transition zone (Loc 16), contrast was also seen in line with the structure of enamel. The 3D tomography data showed significant degradation of the enamel within the depth of the carious lesion and it was also found that at the surface the enamel structure was not as well resolved similar to the non-carious region (Loc 2). However, contrast could be noticed in the tomography data in different regions of Loc 7 (Fig. 7a) suggested from the modification of the structure in comparison with the non-carious region. From the 3D tomography data, visualisation of the interface from the surface to the carious lesion was observed from a large region, Loc 7SI-Fig. S1d and Loc 6,7 in SI-Figs. S31,32. Whereas in the FIB-SEM, the sheath region was resolved and demineralisation was also apparent. The field of view was much larger than the region examined using FIB-SEM and provided a larger view of the cross-sections, slice and view locations, demineralisation and rods and inter-rod structure in the lesion, SI-Figs. S24c,25c,31–39, showing more details which could not be examined with SEM alone, as previously observed[13]. As shown in Fig. 7b, the 3D rendering of the SV1 after milling provided further details on the rod structure deeper in the enamel. The 3D FIB-SEM technique resolution was 40 and 10 times higher (for SV1, and both SV4 and SV5) than the resolution of the tomography using a 10x objective lens resulting in better visualisation of the details and internal structure of rod and inter-rod (summarised in SI-Fig. S37b).

In addition, the large field of view of the tomography provided a larger volume of enamel for analysis which aided tracking of the demineralised structure at the surface, as shown for Loc 7 and Loc 6, SI-Figs. S31,32. Rod structures were visualised with the progression of the virtual slices going further than the surface and compare with the other regions, Loc 9, Loc 2, Loc 16 and Loc 24. Clear differences were found in the carious lesion, as well as non-carious and surface region, SI-Figs. S33–36, SI-Movie S3, movie available on Mendeley Data[70]. These sequences of slices on the tomogram after FIB-SEM milling illustrated the resolution observed on the milled cross-sections. Additionally, this highlighted the transition in the structure of enamel going from the lesion to non-carious region, see Loc 24SI-Fig. S36.

Similar to the analysis of porosity in several locations from the SEM images, measurements were carried out using the tomography data to obtain deeper insight into the distribution of porosity in localised regions of the sample, Fig. 8 and benefiting from the large field of view and internal structure generated by tomography. Based on the locations previously annotated, the sample was locally characterised. Significant differences were found between the average volume of the segmented dataset from the analysed zones (Fig. 8 and SI-Fig. S40; the surface zone is  $0.97 \pm 1.17\%$ ; the body of the lesion with the highest value is  $21.79 \pm 10.85\%$ ; the transition zone is  $3.78 \pm 6.19\%$ ; the non-carious region with the lowest value is  $0.007 \pm 0.026\%$ ). The trend concurs with the FIB-SEM, however the values are different. Lower values were found in the body of lesion as compared with SEM quantification, but as mentioned earlier, volume analysis of both rod and inter-rod structure contributed to the measured region, Fig. 8c, in the overall analysed volume in the synchrotron data. Porosity analysis in small regions was carried out to limit the overlap of modification in the structure. This is detailed with the distance analysis carried out on the surface zone and the analysis of the volume from a larger subregion, SI-Fig. S41.

It was important to localise the region analysed, as inhomogeneities in enamel structure were found with depth in the sample from the lateral coordinate, Fig. 9, SI-Figs. S42–44. The computed tomography measurements analysed the enamel inhomogeneity, which could not be assessed from the light microscopy image, SI-Fig. 42c. To obtain deeper insight into the structure and using the rich data from the tomography, virtual slices extracted at different depths along the z axis in the sample highlighted the organisation of enamel, Fig. 9 and SI-Figs. S42,43. Less structural details were found at the surface and in the non-carious region confirmed with further zooming into specific regions. This revealed a high level of details within the carious sample and clearly illustrated the complexity of the organization of the enamel structure at different locations, the wavy organisation of Hunter-Schreger bands [71] and cracks visualisation, SI-Movie S4 available on Mendeley Data[70]. The lesion was found less intense within the depth (from the z axis of the reconstructed data axis). The lesion was found to follow the structure of the rods from transition to transition zone to non-carious, and curvature of the rods was also observed. As previously reported, a cone shape was mentioned to describe the carious lesion[72], but with observations of the lesion here, this was a general interpretation without considering the internal structure.

Interestingly the observed structures showed transition regions from the body of the lesion to the dentino-enamel junction (DEJ), detailed in Fig. 9b and SI-Fig. S44. It was found that starting from the body of the lesion there was a first zone with strong demineralisation, then a decrease in the demineralisation, followed by alternation pattern of increase decrease and increase in the observed structure towards the DEJ. This suggested the presence of further zones in the lesion in comparison with the traditional description. The presence of at least one more zone compared with the classical histological description concurs with early reports on enamel with an additional zone referred to as a “secondary translucent zone” between the body of the lesion and the dark zone[29] and other denomination[73].

However, a detailed study with more samples would be required to confirm the observations and to determine whether it is specific to this particular sample, or other if there is a ternary translucent, or other dark zones etc. Overall representation of the virtual slices in the sample is illustrated in SI-Movies S5,6 available on Mendeley Data[70]. These transitions were also noticeable with the X-ray laboratory tomography dataset (SI-Fig. S45), but lacked structural details in comparison with the synchrotron data. Further thresholding analysis of the light microscopy image showed also additional details of the zone determination, SI-Fig. S46.

In the other orientation of the virtual slices, Fig. 9c, rods trajectory was visualised with a wavy organisation. Furthermore, this orientation provided direct view of the distribution of the demineralisation with the thickness of the sample. From the larger field of view of the FIB-SEM dataset, the rods were extracted over subregions to identify their trajectory, Fig. 9d and SI-Figs. S47,48, and SI-Movie S7 available on Mendeley Data[70]. From the demineralised structure of enamel and contrast in the tomography dataset, the complexity of the enamel rods organisation was extracted in 3D. The tomography dataset enabled the tracking from different volume dimensions, leading to significant improvement in localised rod structure determination, this was detailed with rods extracted from larger region of the enamel and correlation with virtual slices, SI-Fig. S49. In addition, a significant difference in demineralisation with location along the thickness was shown in SI-Fig. S50 with the surrounding region with less demineralised enamel showing preferential remaining dissolution.

From the tomography data, using the internal structural analysis, dark lines were observed near the surface zone of the enamel. These lines were thought to be the striae of Retzius, which have

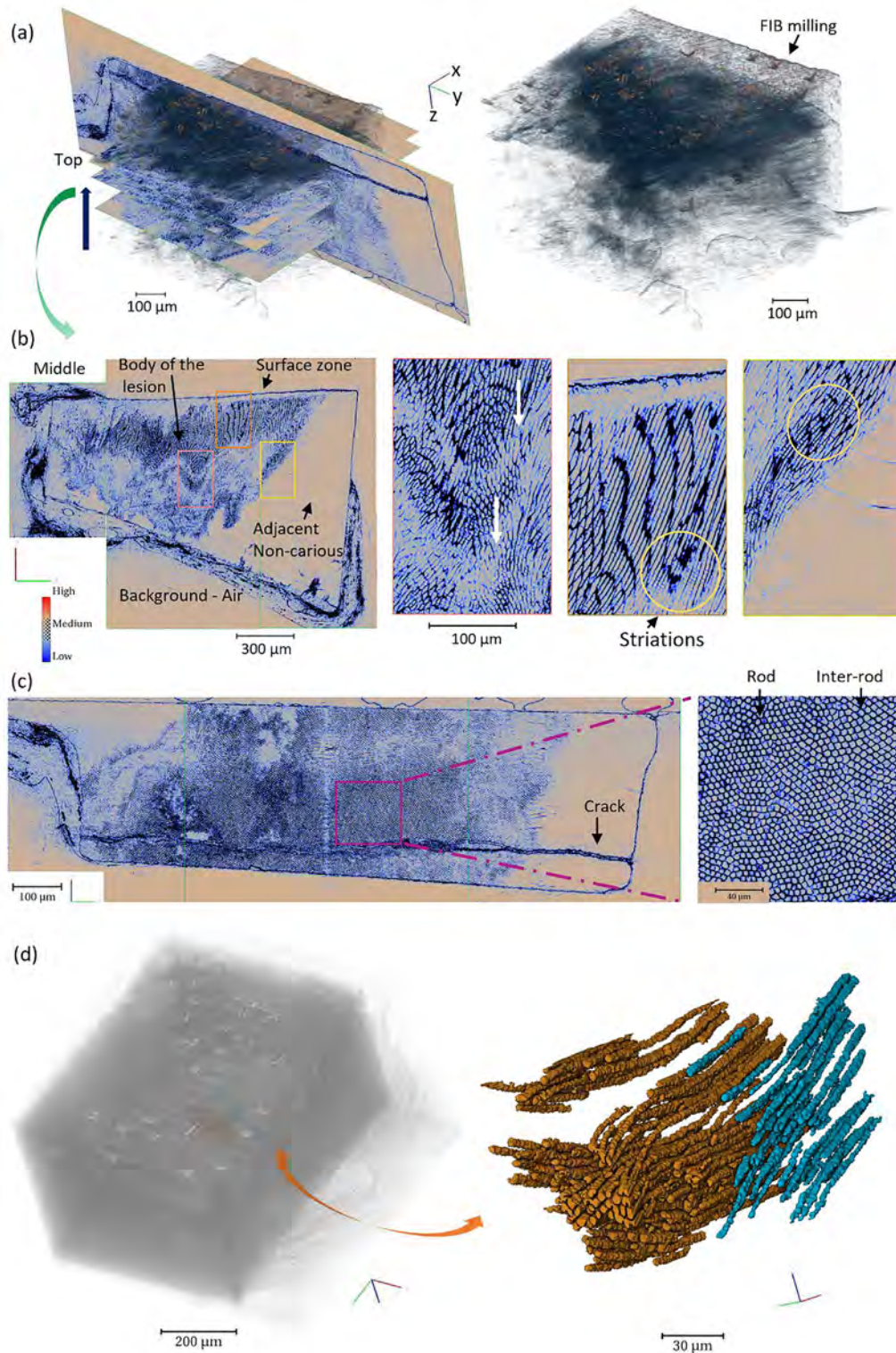


**Fig. 9.** Tomography analysis of a large region of enamel. (a) 3D rendering of the enamel from one of the tomographs and virtual slices in two orientations, datasets after membrane enhancement filter. (b) Montage of the five scans (voxel size 0.325 μm) with virtual slices of enamel (after filtering) at different z value (displayed in (a) from the reconstructed datasets) and the extraction of three subregions of interest in each of the z, the two other slice of (a) are detailed in SI-Fig. S42. This highlights the structure of the rods, inter-rod in the three locations targeting the zones described in the light microscopy image Fig. 4 and SI-Fig. S1a. Transitions in the visualised structure are detailed with arrows, and striations highlighted. (c) Virtual slices in yz orientation with the observation of the structure of enamel with a view more perpendicular to the rods axis than (b), zoom in SI-Fig. S43. (d) 3D rendering of one tomogram (815.425 × 815.425 × 587.925 μm, 2510 × 2510 × 1810 pixels) with the superimposition of a subvolume (203.775 × 203.775 × 129.675 μm, 628 × 628 × 400 pixels) of the structure of enamel after membrane enhancement filter, 3D median filter and segmentation (segmentation carried out using segmentation tools and editor). Zoom in the subvolume that detailed the observation of the complex pathway of the rods, supplemental details in SI-Fig. S47. Additional details of the virtual slices in the montage before and after membrane enhancement filter in SI-Movies S5-7 available on Mendeley Data[70].



been previously reported to be more noticeable in demineralised enamel and also possibly demonstrate a preferential demineralisation pathway[23,74–77]. These have lower grey values as compared to with the neighbouring regions, which suggested that these lines were more susceptible to acid demineralisation. These regions have 3D organisation, which was seen in the illustration of three virtual slices and the volume of a subregion, SI-Fig. S51a. Preferential demineralised regions in and near the surface zone were observed and could correspond with preferential entry of the dissolution process of acid. The surface zone, based on the resolution and contrast of the tomography dataset could also be quantified, this is illustrated for one slice, SI-Fig S52 with a dimension which varies along the  $x$  axis.

Further analysis of observed features in the tomography dataset revealed cross-striation in the rods with lines cutting the main axis of the rods, SI-Fig. 53. These striations were previously visualised in the projections data from synchrotron tomography acquisition and their origin mentioned elsewhere[13]. From the observation of these striations in the carious lesion, it is suggested that they have a role in the carious process arising from the difference in the degradation of the structure compared with surrounding material.

To summarise the importance of correlative analysis[78], overall correlative analysis was done with SEM and tomography imaging mode and light microscopy, SI-Fig. S54a–c. The zones determined from the light microscopy image can be used to extract zones with their corresponding volumes in the tomography data in a similar approach as used in the SEM correlative analysis with the light microscopy image. This approach led to an approximation (considering that this is based on a 2D image and that the light microscopy image of the carious sample from the other face differs[13]) of the whole structure present in each visualised zone as compared with the classical analysis based on 2D images obtained using light microscopy. From the zones, 3D visualisation of the region referred to as the body of lesion from the light microscopy image was extracted (SI-Fig. 54d) and this confirmed the limitation in the light microscopy image to reveal the volume of porosity, because as seen from the stack of reconstructed slices, it was found that the lesion had variations along the thickness of the sample with less important demineralisation at the bottom from the visualisation of the tomography data.

The correlative analysis gave new insights into the structure of carious enamel providing further information about the lesion, additional axis of research could be studied, structural[4] and chemical analysis (such as X-ray fluorescence spectroscopy[79]), protein analysis[80], other samples with different degree of caries, and artificially demineralised samples to evaluate the mimicry of caries and other techniques e.g., optical coherence tomography[81], small-angle X-ray scattering[82].

## 2.6. Scanning transmission electron microscopy (STEM)

To enhance spatial resolution, STEM analysis in SEM was performed on thin enamel lamellae using bright and dark field modalities and the different origins of transmitted electrons, at both low angles and high angles respectively[83]. These provided structural details of the crystallites, pores at the nanoscale prior to further TEM analysis. A high-density of crystallites was identified on the analysed lamellae from Loc 14 and Loc 23 located in the transition zone. The crystallites had an inhomogeneous organisation, see Fig. 10 and SI-Figs. S55,56. Using bright field, identification of crystallites was undertaken using the variation of contrast between neighbouring crystallites. With this analysis, highly packed crystallite organisation was observed and a curvature in the arrangement of the crystallites was noticed. The distribution of pores was visualised with bright region with heterogeneity of shape, as

well as vertical bands due to the FIB processing (curtaining effect). The sheath region was identified on the lamella with clear observation of variation of thickness and discontinuity in the surrounding of the rod structure as mentioned before. The boundary of the sheath followed the shape of the crystallites. Contrast variation of some crystallites using the same setting in bright field images seen as darker regions were identified on the dark field images and related to crystallites. More details were observed within crystallites using dark field as well as additional interfaces. In dark field images, pores were observed with dark regions, in contrast to bright field. Variation of image contrast was also seen in the crystallites (region darker than surrounding) and could be related to the preferential demineralisation locations within the core of the crystallites.

To go further in the analysis of Loc 14, STEM using TEM and high-angle annular dark field (HAADF) imaging and spectroscopy preliminarily analysis with EDS and electron energy loss spectroscopy (EELS) were carried out. From the EDS spectrum and mapping, Ca, P elements were found as well as F, SI-Fig. S57a–d, as previously detected on fluoridated enamel[20]. The detection of these elements using TEM spectroscopy suggests that the method is applicable on thin sample and could later be used to compare chemical composition across locations. EELS analysis was also carried out and showed the peak positions for Ca L-edge and P L-edge. The results for Ca are illustrated in SI-Fig. S57.

The multi-scale correlative approach reveals the details that could not be seen with the conventional light microscopy and/or laboratory tomography, whilst preserving specific reference to precise locations within the carious enamel lesion and its zones. Thus, the various techniques are connected across a range of scales of description from micro-features in light microscopy through non-destructive laboratory X-ray microtomography and sub-micron synchrotron tomography down to the 2D and 3D nanoscale FIB-SEM and to the highest resolution using STEM, Fig. 1.

## 3. Conclusion

The hierarchical structure of carious enamel and localised demineralised regions were revealed in 2D and 3D using correlative imaging technique providing details to revisit the characteristic of the lesion. Light microscopy image enabled determining the classical histology of enamel carious zones which was used to localise regions in other imaging modes based on correlative imaging analysis. The use of two beams in FIB-SEM provided localised nanoscale 2D/3D imaging method and further quantification revealing ultra-structural subsurface changes in enamel caries at high-resolution prior to TEM analysis which has not been described previously. High-resolution imaging of surface enamel highlighted the complex structure of this zone with a less porous structure than deeper carious locations, where degradations of the structure were evident in both rods and inter-rod in the carious region. Significant differences were obtained in the quantification of porosity from the zones described for enamel caries, the surface zone, body of the lesion, transition zone and non-carious region, from the SEM images. The sheath region was found with discontinuity around the rods. Connected porosity regions were revealed using the 3D FIB-SEM and the slice and view process showed the progression of the voids and internal network of porosities within the carious lesion.

Synchrotron X-ray tomography, even though with a lower resolution than SEM, provided 3D and 2D images with enough details to visualise rods and inter-rods, and lead to an unprecedented view of the complexity of the enamel structure, surface and internally with a resolution down to 0.325  $\mu\text{m}$ . A montage from several data was made to examine the full sample, localised region were

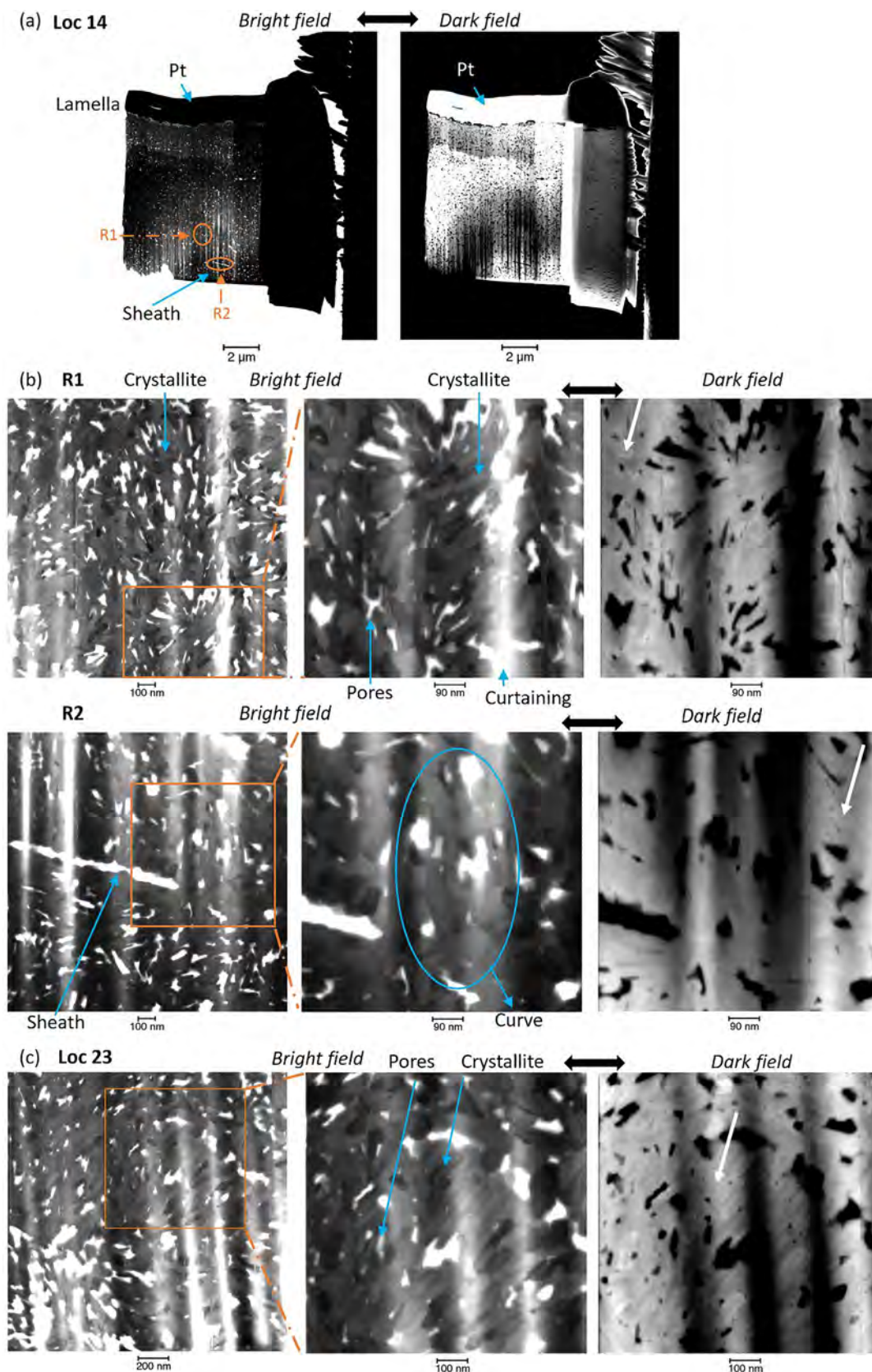


**Fig. 10.** STEM images of enamel caries in Loc 14 and Loc 23 (located in the transition zone) using bright field and dark field imaging technique. (a) Low magnification of bright field and dark field image of the lamella of Loc 14 after lifting and polishing, highlights are for two regions of interest with sheath and crystallites visualisation, R1 and R2. Platinum remaining was also observed. (b) Bright-field images of the zoom-in in the three regions with identification of highly packed crystallite organisation, non-straight path, irregularities of the sheath structure and in bright contrast, the pores as well as vertical bright light resulting from the FIB process, curtaining effect. In the dark field image of R1 and R2, contrast variations were seen within the crystallites (highlighted with white arrows), which was sharper than the corresponding bright field images, and more interfaces were visualised. (c) Additional STEM analysis for Loc 14 and another location Loc 23 can be seen in SI-Figs. S55,56.



extracted from each tomogram and the quantification of the demineralisation from subvolumes was found to be significantly inhomogeneous across the zones. The demineralisation in carious enamel in comparison with normal enamel enabled the characterisation of rods, inter-rods, striations, Hunter-Schreger bands and the surface zone. Using the synchrotron tomography, additional zones (compared with the traditional zones) were identified within the thickness of the sample. It is possible to identify the pathways of the rods with high-resolution within the lesions in 2D from virtual slices and 3D. This novel combination of both dataset with direct correlation of SEM images and synchrotron tomography data provided an enhanced view of the hierarchical structure of enamel. Dark field images in STEM aided in the identification of contrast variation within crystallites, potential preferential locations of demineralisation and voids were identified which were similar to those seen in bright field images. STEM (in TEM) with spectroscopy analysis provided elemental details on Ca, P and F which could be extended to other locations for comparison.

We provided a platform for monitoring ultra-structural changes occur in the sample that enables subsequent tracking of these changes during de-/re-mineralisation *in vitro* on extracted teeth, arrested caries across the scales or other enamel disease. Additionally, the fast acquisition of the tomography provided a benefit in time process analysis. This platform allows dental research in caries therapy to develop more reliable therapeutic approaches, potential future materials used in clinical practice, with the new insights on the structure. The methods can be transferred to other dental tissue targeting modification of the tissue up to 0.325  $\mu\text{m}$  over large regions, and with higher resolution in smaller regions.

The principal conclusions drawn from the current study are:

- A micro/nano-histological analysis of human carious enamel was described using correlative imaging.
- Localised analysis of the enamel structure revealed inhomogeneous features in caries.
- Significant differences in 2D and 3D porosity between different zones in carious enamel were demonstrated via qualitative and quantitative statistical analysis.
- A multi-scale platform for characterising enamel is transferable to other applications in dental research.

## 4. Methods

### 4.1. Sample preparation and light microscopy

The sample used was from a human molar extracted for non-carries associated therapeutic reasons at the School of Dentistry, University of Birmingham (ethical approval obtained from the National Research Ethics Committee; NHS-REC reference 14/EM/1128/ Consortium Reference BCHCDent332.1531.TB, the tooth was anonymised). A block cut from the tooth with caries was previously imaged with light microscopy (image was described in our previous work[13]) in air prior to FIB-SEM. The light microscopy image was used to determine different regions (zones) in carious enamel. The sample was then coated with  $\sim 20$  nm of gold (Au) and palladium (Pd) using SC7620 sputter coater (Quorum Technologies, U.K.). Silver paint was spread on the side of the sample, to reduce electron charging in the SEM. Additional details of the sample preparation has been reported previously[13].

### 4.2. FIB-SEM milling preparation

Secondary and backscattered electron images (SEi and BSi) and STEM images were acquired using SEM Tescan Lyra 3 (Tescan, Czech Republic) using an accelerating voltage from 2 to 30 keV. A focused ion beam with the gallium (Ga) source was used at

30 kV with an emission current of  $\sim 2$   $\mu\text{A}$  at the angle of incidence  $55^\circ$  between the FIB and electron beam (SI-Fig. S1e). Elemental analysis in the SEM, energy-dispersive X-ray spectroscopy (EDS), was performed using X-Max 150 EDS detector (Oxford Instruments, U.K.), line scan and point analysis were carried out and interpreted using Aztec Oxford Instruments software. The details of the data interpretation, including the influence of the interaction volume and effect of enamel density have been reported previously [4].

Thin cross sections ( $\sim 2$   $\mu\text{m}$ ) were made using FIB and imaging was carried out through all steps of the process starting from platinum (Pt) deposition to the final ion beam thinning. Orientation of the cross-sections were determined following a previous tomography and SEM images of the sample[13], and most of the cross-sections were chosen to be close to the parallel of the long axis of enamel rods. Several locations were analysed, and to create these cross-sections (and lamella), Pt was deposited, then a marker was milled for the drift correction, followed by trenches made on both side of the Pt deposition with a drift correction during the process. Furthermore, thinning was carried out to achieve the required dimensions, using another drift correction marker, see SI-Fig. S58 for the summary of steps for one representative location and SI-Table S2 for the current used. The effect of the FIB probe current on the structure of carious and non-carious enamel was discussed in our previous publication[13], illustrating that different locations in enamel can be compared using similar methods in the milling and thinning of enamel. The distribution profile of the Ga ion with the HAp was simulated using SRIM 2013 software[84], see SI-Fig. S59, highlighting the importance to protect the surface of the sample. The acquired two-dimensional (2D) SEM and FIB images were analysed using Avizo software (Thermo Fisher Scientific, USA)[85], and the colour maps were adjusted if required for better visualisation.

### 4.3. 2D analysis using FIB-SEM and light microscopy image correlation

For precise localisation of the cross-sections and the FIB-SEM 3D datasets (slice and view) in the examined regions, a SEM image was correlated with the light microscopy image to allow identification of the sample region affected by caries and distinctive zones in the structure of carious enamel. To extract the zones, the light microscopy image was converted into greyscale, then filtered (median filter) and then the segmentation was carried out with four ranges of grey value to extract the region of interest of enamel, SI-Fig. S1a. The process was done using segmentation tools and editor in Avizo. Several regions in the carious lesion were investigated; the surface zone of enamel, the body of the lesion as well as adjacent non-carious enamel (normal enamel). Then transition regions (two zones) were found from body of the lesion to non-carious enamel and for the analysis of the milled locations, these two regions were combined and referred to as 'transition zone' in this study (it could have a part of the condensation zone as reported earlier[9]). In summary, a yellow colour was assigned to the non-carious region, cyan and red to the transition zone, and red also combining the surface zone, and blue the body of the lesion, see Fig. 4. There is uncertainty in the determination of these zones due to variation of contrast in the image which is not sharp and differences in the analysis from the medium used in optical imaging[86] (for instance, in air, dark and translucent zone could be less obvious than when mounted in quinolone[25]), also seen in artificial demineralisation enamel[87].

One artefact known to arise from the FIB process is the 'curtaining' effect leading to vertical bands after FIB milling. A fast Fourier transform (FFT) filter module in Avizo was used to reduce this artefact if necessary (SI-Fig. S15), with vertical orientation for the stripes.

The segmentation and quantification of the sheath region in enamel were carried out by computing FFT filter on BSi, followed by filtering using a machine learning procedure that consisted of a deep learning predictor, (referred to as 'AI' in this document) based on the study from Ronneberger et al.[88,89] and which is available in Avizo software. Shadowing correction was carried out when required. Binarisation was done with the 'Segmentation editor' in Avizo which performed thresholding and additional cleaning steps to remove segments not in the region of interest.

Porosity analysis was carried out in more than twenty FIB-SEM cross-sections locations which were assigned in the zones determined with the light microscopy image. Subregions of the BSi suggested to be located more in the rods than inter-rod based on the enamel structure seen were statistically analysed. The porosity was extracted by segmentation on the filtered data. Same dimension for each subregion was analysed. A summary of the process from raw data to quantifications with all possible performed corrections on an image which could be done is detailed in SI-Fig. S15. The total segmented area was the sum of all individual segments. Furthermore, a comparison of porosity analysis was carried out between rods and inter-rod for one location.

Quantification of the spacing region between pores was carried out using Euclidean distance transform[13]. A summary of the analysis is detailed in SI-Fig. S15. Rod morphology was quantified in a several locations after segmentation using a 'lasso' tool to extract the contour of the region of interest, SI-Fig. S13 and referred to as 'radius' to distinguish it from the Euclidean distance mentioned earlier. Matlab and OriginPro software were used to analyse and plot the data.

To visualise rods in different cross section orientations, Loc 8 was prepared to be close to the perpendicular to locations (here referred to as 'longitudinal'). The trajectory of the structure of the remaining material and measurement of orientation angles were carried out on BSi using Avizo, by applying computation of FFT to reduce curtaining artefact, denoising of the new data with AI filter, extraction of the bright structures using the module 'membrane enhancement filter'[90] and manual segmentation of these structures, summarised SI-Fig. S21. This was finally classified from SEM image into rod and inter-rod regions and then the orientation measurement was carried out using the inertia moments in Avizo.

In Loc 8, connected material between enamel structures referred to as 'bridges' were observed and manually measured in several regions of SEi. This was carried out by measuring the dimension from the 2D section after Gaussian filtering to reduce noise (summarised SI-Fig. S22b), subsequent statistical analysis was also carried out on the measured dimensions.

#### 4.4. 3D analysis using FIB-SEM

Nanoscale 3D view of porosities in carious regions and detailed enamel structure was achieved using FIB-SEM 3D (also referred to as slice and view) technique. Five locations were analysed in the carious region to highlight the potential of this method for caries analysis. Pt was first deposited, then trenches were milled on the front and side of the region of interest (using 3D wizard and additional freeform for one location), then thinning steps were carried out to clean the rough milling using drift correction. For the slice and view, 3D wizard implemented in Lyra software was used, with markers placed to account for drift, then the slicing was carried out, with voxel sizes of 29 and 8 nm. SEi and BSi were then simultaneously acquired to limit missing data. During the acquisition of the images, a foreshortening correction[91] was carried out in the microscope software with the tilt and dynamic rotation enabled to compensate for the tilt stage (similar as acquisition of some

cross-section images). The slice and view preparation is summarised in SI-Fig. S60.

Raw data BSi from the slice and view acquisition were filtered with FFT, then aligned using fiducial landmarks that were manually placed on each slice and using module align from Avizo. A shearing correction was applied with an angle of  $-35^\circ$  to account for the tilt of the stage using FIB wizard. Denoising of the images was computed out by conserving the edges of the observed structures using AI. Five slice and view locations were milled and referred to as SV1-SV5, the voxel size was  $\sim 8$  nm for SV1 and  $\sim 29$  nm for the other. Segmentation of the porosity volumes was done and further quantified for cluster and connectivity analysis. Distance analysis of the spacing region between pores was also computed using Avizo.

#### 4.5. STEM in SEM imaging

The lift out of lamella was carried out from two cross-section locations and the lamella was attached to copper (Cu) grid using a nanomanipulator. An undercut was milled on the sample, then a connection was created between the needle and the lamella (using Pt deposition). Then a cut was performed on the unconnected side of the lamella. The lamella was then brought to the Cu grid, attached with Pt and cut free from the nanomanipulator. The sample was then thinned with various tilt angles ( $\pm 2^\circ$ ) and then a final polishing was carried out with a voltage of 5 kV, and tilt angles  $\pm 6^\circ$ . The sequence of steps is shown in SI-Fig. S61, and the summary of the settings SI-Table S2. In SEM (30 keV) a STEM detector was inserted and bright and dark field images of the lamella were acquired.

#### 4.6. TEM/STEM, EELS and EDS analysis

Loc 14 was analysed using TEM/STEM and HAADF imaging. This was carried out in The electron Physical Science Imaging Centre (ePSIC) in Diamond Light Source (DLS), Oxford Harwell Campus, Didcot, U.K. Imaging HAADF was carried out with an accelerating voltage of 200 keV, with beam current of 41 pA using JEOL ARM200CF. The same instrument was used for spectroscopy analysis. EDS was performed with a voltage of 200 keV, and mapping as well as spectra acquired with Digital Micrograph software, 0.01 keV/ch, and on the other hand EELS was carried out with a voltage of 200 keV and 0.5 eV/ch. EELS spectrum and background removal was carried out with Digital Micrograph and HyperSpy softwares[92].

#### 4.7. Synchrotron X-ray tomography setup

Synchrotron X-ray tomography was performed at the I13-2 beamline (DLS)[93–95]. The sample was analysed after mounting on a SEM stub and acquisition performed at room temperature using pink X-ray beam of average energy of  $31 \text{ keV} \pm 5 \text{ keV}$ , with pyrolytic graphite (1.34 mm) and aluminium (3.2 mm), and 150  $\mu\text{m}$  iron filters. The detector used to acquire the data was pco.edge 5.5 (PCO AG, Germany) CMOS sensor. Two objective lenses were used (4x and 10x), with a field of view of  $2560 \times 2160$  pixels ( $2079.19 \times 1754.19 \mu\text{m}$  and  $831.675 \times 701.675 \mu\text{m}$  and voxel size of  $0.8125 \mu\text{m}$  and  $0.325 \mu\text{m}$  respectively). The distance from the scintillator screen to the sample was 135 and 35 mm, respectively. For both objectives, a rotation was done from 0 to  $180^\circ$ , at angular step of  $0.051^\circ$ , 40 dark field and flat field images were acquired prior to the acquisition of the sample images (for subsequent background correction). An exposure time of 0.3 s and 0.5 s were used for the 4x and the 10x objectives respectively. A total of 3610 images were acquired per each scan. The reconstruction was carried out using Savu software and bespoke plug-



ins and scripts (I13-2 beamline and Savu)[96,97] in line with our previous study [13]. For the data acquired with the objective lenses, the reconstruction led to volumes of  $2038.56 \times 2038.56 \times 1713.56 \mu\text{m}^3$  and  $815.425 \times 815.425 \times 685.425 \mu\text{m}^3$  ( $2510 \times 2510 \times 2110$  pixels), where multiple regions of interest were virtually extracted corresponding with specific locations, such as FIB-SEM cross-sections. Five scans were carried out to examine the entire sample using 10x objective lens. The scans were carried out after that some FIB-SEM milling regions were made (either remaining trench after slice and view or lift-out of lamella, before or after undercut). Pt with higher density than enamel, lead to high absorbance observed on the dataset which for some regions allow direct localisation.

#### 4.8. Synchrotron and laboratory X-ray tomography analysis and correlation with light microscopy and SEM images

The projection images, 3D renderings of synchrotron data were done at 16 bits greyscale and the analysis of data was carried out using DAWN[98], ImageJ-Fiji[99,100], and Avizo packages with rendering, filtering etc following our previous work [13]. Correlation between the synchrotron data and SEM images was carried out by identifying the same locations of the sample and superimposing the images from both modalities (BSi and filtered tomographic datasets) using Avizo. In addition, several 3D rendering of the several locations before or after FIB-milling were extracted to highlight the structure. To cover the full block of enamel, the five reconstructed data were rearranged to produce one rich dataset. One of the ways to illustrate the structure of enamel was to use 'membrane enhancement filter' previously mentioned on the bright features (the aim was to target the remaining materials, inter-rods), see SI-Fig. S62 and SI-Movies S8,9 available on Mendeley Data[70]. This was also used to extract the pathway of rods.

Porosity analysis was carried out in several regions based on the locations determined with FIB-SEM. Considering that many locations were already milled, the porosity was determined at higher depth in numerous locations in the sample with lateral coordinates based on the SEM locations. For each analysed location, three regions were extracted at different depths with same volume ( $12.675 \times 12.675 \times 12.675 \mu\text{m}^3$  and large subregions  $64.7 \times 64.7 \times 48.4 \mu\text{m}^3$ ). The analysis was done after filtering the data of three reconstructed tomograms (each volume  $815.425 \times 815.425 \times 587.925 \mu\text{m}^3$ ,  $2510 \times 2510 \times 1810$  pixels, voxel size  $0.325 \mu\text{m}$ ) using 3D median filter, and then extraction of the subregions and binarisation of the regions to extract the low grey value and the volume fraction. For the locations at the surface, the lateral coordinates were significantly modified due to the shape of the sample to cover sample material without any background. The small subregions were contained in the x and y coordinates of the large regions based on the SEM locations.

Similar to the superimposition carried out from the light microscopy image and SEM, manual correlation was done on the tomography data and the two other imaging mode. For SEM and X-ray tomography, FIB-SEM locations already made were used to correlate the dataset, and the edges of the SEM sample for the light microscopy image. This led to overall correlation from the different imaging modes.

Laboratory tomography data were analysed and virtual slices were extracted from the tomogram previously acquired with voxel size of  $1.51 \mu\text{m}$  [13]. The details of the sample imaged with both tomography experiment is shown in SI-Fig. S1b-d.

#### 4.9. Statistical analysis

One-way ANOVA with post hoc Tukey's test was used in the study (OriginPro software) and annotated in figure captions. A p-

value  $< 0.05$  was considered statistically significant. \* represents  $p < 0.05$ , \*\* represents  $p \leq 0.01$ , \*\*\* represents  $p \leq 0.001$ , and \*\*\*\* represents  $p \leq 0.0001$ .

#### Data availability statement

Data collected and interpreted in this study is maintained by the authors and can be made available upon request. A representative original dataset is accessible in the form of a stack of raw slices from tomographic reconstruction (non-filtered) at the voxel size  $0.325$  of  $0.325 \mu\text{m}$ .

#### CRediT authorship contribution statement

Alexander M. Korsunsky and Cyril Besnard Conceptualization, Supervision with Gabriel Landini and Richard M. Shelton. Cyril Besnard, Ali Marie, Robert A. Harper, Shashidhara Marathe and Kaz Wanelik Methodology, Data curation in the synchrotron beamtime. Cyril Besnard Investigation, Methodology, Data curation, performed EDS and SEM/FIB-SEM/STEM analysis with support of Petr Buček. Cyril Besnard Investigation, Methodology, Formal analysis, Software, Visualization, analysed the data from the synchrotron X-ray tomography, laboratory tomography, SEM/FIB-SEM/STEM (from SEM)/EDS, and initially created all the figures and movies. Cyril Besnard Writing - Original Draft and Cyril Besnard, Ali Marie, Sisini Sasidharan, Robert A. Harper, Petr Buček, Shashidhara Marathe, Kaz Wanelik, Gabriel Landini, Richard M. Shelton, and Alexander M. Korsunsky Writing - Review & Editing.

#### Declaration of Competing Interest

The authors declare the following financial interests/personal relationships which may be considered as potential competing interests: Prof. Alexander M. Korsunsky Editor-in-Chief of JMADE.

#### Acknowledgement

This work was primary funded by The Engineering and Physical Sciences Research Council (EPSRC) entitled "Tackling human dental caries by multi-modal correlative microscopy and multi-physics modelling" (EP/P005381/1) and "Rich Nonlinear Tomography for advanced materials" (EP/V007785/1). S.S and A.M appreciate the support of the Health Research Bridging Salary Scheme (BRR00060-DF02 and BRR00060-DF03, respectively) by the Medical Science Divisions, University of Oxford. Synchrotron tomography acquisitions were performed thanks to I13 beamline in Diamond Light Source for the access under the proposal mg29256-2 and data beamline access, thanks to I13 Beamline team Prof. Christophe Rau and Dr Andrew Bodey (Diamond Light Source Ltd., Didcot, Oxfordshire, OX11 0DE, U.K.). Thanks to the support for Avizo from the Materials & Structural Analysis team from Thermo Fisher Scientific. We thank Dr Chia-Chen Hsu for the discussion on the statistical analysis. We thank Diamond Light Source for access and support in use of the electron Physical Science Imaging Centre (Instrument E01, proposal number MG30666) for TEM/EELS/EDS carried out by Dr Christopher Allen (Electron Physical Sciences Imaging Centre, Diamond Light Source Ltd., Didcot, Oxfordshire, OX11 0DE, U.K. and Department of Materials, University of Oxford, Oxford, OX1 3PH, U.K.) that contributed to the results presented here.

#### Appendix A. Supplementary material

Supplementary data to this article can be found online at <https://doi.org/10.1016/j.matdes.2022.110829>.

## References

- [1] M.A. Peres, L.M.D. Macpherson, R.J. Weyant, B. Daly, R. Venturelli, M.R. Mathur, S. Listl, R.K. Celeste, C.C. Guarnizo-Herreño, C. Kearns, H. Benzan, P. Allison, R.G. Watt, Oral diseases: a global public health challenge, *The Lancet* 394 (10194) (2019) 249–260, [https://doi.org/10.1016/S0140-6736\(19\)31146-8](https://doi.org/10.1016/S0140-6736(19)31146-8).
- [2] D.J. Manton, Child dental caries – A global problem of inequality, *EClinicalMedicine* 1 (2018) 3–4, <https://doi.org/10.1016/j.eclinm.2018.06.006>.
- [3] S. Risnes, C. Li, On the method of revealing enamel structure by acid etching. Aspects of optimization and interpretation, *Microsc. Res. Tech.* 82 (10) (2019) 1668–1680, <https://doi.org/10.1002/jemt.23333>.
- [4] C. Besnard, R.A. Harper, E. Salvati, T.E.J. Moxham, L. Romano Brandt, G. Landini, R.M. Shelton, A.M. Korsunsky, Analysis of *in vitro* demineralised human enamel using multi-scale correlative optical and scanning electron microscopy, and high-resolution synchrotron wide-angle X-ray scattering, *Mater. Des.* 206 (2021) 109739, <https://doi.org/10.1016/j.matdes.2021.109739>.
- [5] M. Eisenburger, R.P. Shellis, M. Addy, Scanning electron microscopy of softened enamel, *Caries Res.* 38 (2004) 67–74, <https://doi.org/10.1159/000073923>.
- [6] Y.J. Yoon, I.-H. Kim, S.-Y. Han, The reason why a sheath exists in enamel, *Int. J. Precis. Eng. Manuf.* 16 (4) (2015) 807–811, <https://doi.org/10.1007/s12541-015-0106-1>.
- [7] R.Z. Legeros, Chemical and crystallographic events in the caries process, *J. Dent. Res.* 69 (2\_suppl) (1990) 567–574, <https://doi.org/10.1177/002203459006905113>.
- [8] J.D.B. Featherstone, Dental caries: a dynamic disease process, *Aust. Dent. J.* 53 (2008) 286–291, <https://doi.org/10.1111/j.1834-7819.2008.00064.x>.
- [9] M. Goldberg, Deciduous tooth and dental caries, *Ann. Pediatrics Child Health* 5 (2017) 1120.
- [10] M. Goldberg, Enamel softening (dental erosion) – enamel etching – the early enamel carious lesion in *Understanding Dental Caries* (ed Michel Goldberg) Ch. 2–4, 2016.
- [11] D.B. Scott, J.W. Simmelink, V. Nygaard, Structural aspects of dental caries, *J. Dent. Res.* 53 (2) (1974) 165–178, <https://doi.org/10.1177/00220345740530020401>.
- [12] E.I.F. Pearce, D.G.A. Nelson, Microstructural features of carious human enamel imaged with back-scattered electrons, *J. Dent. Res.* 68 (2) (1989) 113–118, <https://doi.org/10.1177/00220345890680020301>.
- [13] C. Besnard, R.A. Harper, T.E.J. Moxham, J.D. James, M. Storm, E. Salvati, G. Landini, R.M. Shelton, A.M. Korsunsky, 3D analysis of enamel demineralisation in human dental caries using high-resolution, large field of view synchrotron X-ray micro-computed tomography, *Mater. Today Commun.* 27 (2021) 102418, <https://doi.org/10.1016/j.mtcomm.2021.102418>.
- [14] E.F. Bres, J.C. Barry, J.L. Hutchison, A structural basis for the carious dissolution of the apatite crystals of human tooth enamel, *Ultramicroscopy* 12 (4) (1983) 367–371, [https://doi.org/10.1016/0304-3991\(83\)90250-4](https://doi.org/10.1016/0304-3991(83)90250-4).
- [15] L.M. Silverstone, C.A. Saxton, I.L. Dogon, O. Fejerskov, Variation in the pattern of acid etching of human dental enamel examined by scanning electron microscopy, *Caries Res.* 9 (5) (1975) 373–387, <https://doi.org/10.1159/000260179>.
- [16] N.W. Johnson, Transmission electron microscopy of early carious enamel, *Caries Res.* 1 (4) (1967) 356–369, <https://doi.org/10.1159/000259536>.
- [17] T. Yanagisawa, Y. Miake, High-resolution electron microscopy of enamel-crystal demineralization and remineralization in carious lesions, *J. Electron Microsc.* 52 (2003) 605–613.
- [18] R.M. Frank, Microscopie électronique de la carie des sillons chez l'homme, *Arch. Oral Biol.* 18 (1) (1973) 9–25, [https://doi.org/10.1016/0003-9969\(73\)90015-0](https://doi.org/10.1016/0003-9969(73)90015-0).
- [19] A. La Fontaine, A. Zavgorodniy, H. Liu, R. Zheng, M. Swain, J. Cairney, Atomic-scale compositional mapping reveals Mg-rich amorphous calcium phosphate in human dental enamel, *Sci. Adv.* 2 (9) (2016), <https://doi.org/10.1126/sciadv.1601145>.
- [20] K.A. DeRocher, P.J.M. Smeets, B.H. Goodge, M.J. Zachman, P.V. Balachandran, L. Stegbauer, M.J. Cohen, L.M. Gordon, J.M. Rondinelli, L.F. Kourkoutis, D. Joester, Chemical gradients in human enamel crystallites, *Nature* 583 (7814) (2020) 66–71, <https://doi.org/10.1038/s41586-020-2433-3>.
- [21] F. Yun, M.V. Swain, H. Chen, J. Cairney, J. Qu, G. Sha, H. Liu, S.P. Ringer, Y.u. Han, L. Liu, X. Zhang, R. Zheng, Nanoscale pathways for human tooth decay – Central planar defect, organic-rich precipitate and high-angle grain boundary, *Biomaterials* 235 (2020) 119748, <https://doi.org/10.1016/j.biomaterials.2019.119748>.
- [22] W. Shulin, Human enamel structure studied by high resolution electron microscopy, *Electron Microscopy Rev.* 2 (1) (1989) 1–16, [https://doi.org/10.1016/0892-0354\(89\)90008-7](https://doi.org/10.1016/0892-0354(89)90008-7).
- [23] A.I. Darling, Studies of the early lesion of enamel caries with transmitted light, polarized light and microradiography, *Brit. Dental J.* 101, 289–297 and 329–341 (1956).
- [24] A.I. Darling, H.S.M. Crabb, X-ray absorption studies of human dental enamel, *Oral Surgery, Oral Med., Oral Pathol.* 9 (9) (1956) 995–1009, [https://doi.org/10.1016/0030-4220\(56\)90303-6](https://doi.org/10.1016/0030-4220(56)90303-6).
- [25] A.I. Darling, Studies of the early lesion of enamel caries. Its nature, mode of spread, points of entry, *Brit. Dental J.* 105 (1958) 119–135.
- [26] A.I. Darling, K.V. Mortimer, D.F.G. Poole, W.D. Ollis, Molecular sieve behaviour of normal and carious human dental enamel, *Arch. Oral Biol.* 5 (3–4) (1961) 251–273, [https://doi.org/10.1016/0003-9969\(61\)90063-2](https://doi.org/10.1016/0003-9969(61)90063-2).
- [27] D.F.G. Poole, K.V. Mortimer, A.I. Darling, W.D. Ollis, Molecular sieve behaviour of dental enamel, *Nature* 189 (4769) (1961) 998–1000, <https://doi.org/10.1038/189998a0>.
- [28] H.S.M. Crabb, K.V. Mortimer, Dental caries and enamel structure, *Nature* 209 (5023) (1966) 611–612, <https://doi.org/10.1038/209611a0>.
- [29] H.S. Crabb, Enamel caries. Observations on the histology and pattern of progress of the approximal lesion, *Brit. Dental J.* 121, 115–1contd (1966).
- [30] A.I. Darling, The selective attack of caries on the dental enamel, *Ann. R. Coll. Surg. Engl.* 29 (1961) 354–369.
- [31] M. Sezen, Focused Ion Beams (FIB) – Novel Methodologies and Recent Applications for Multidisciplinary Sciences, in: M. Janacek, R. Kral (Eds.), *Modern Electron Microscopy in Physical and Life Sciences*, InTech, 2016, <https://doi.org/10.5772/61634>.
- [32] J. Syed, Scanning electron microscopy in oral research, *J. Pakistan Dental Assoc.* 26 (4) (2018) 189–195.
- [33] S. Weiner, E. Raguin, R. Shahar, High resolution 3D structures of mineralized tissues in health and disease, *Nature Rev. Endocrinol.* 17 (5) (2021) 307–316, <https://doi.org/10.1038/s41574-021-00479-0>.
- [34] N. Nan, J. Wang, FIB-SEM three-dimensional tomography for characterization of carbon-based materials, *Adv. Mater. Sci. Eng.* 2019 (2019) 1–8, <https://doi.org/10.1155/2019/8680715>.
- [35] M. Milani, D. Drobne, F. Tatti, How to study biological samples by FIB / SEM?, in: A. Méndez-Vilas, J. Díaz (Eds.), *Modern Research and Educational Topics in Microscopy*, vol. (2), pp. 787–794 (FORMATX, 2007).
- [36] C. Xie, L. Hanson, W. Xie, Z. Lin, B. Cui, Y.i. Cui, Noninvasive neuron pinning with nanopillar arrays, *Nano Lett.* 10 (10) (2010) 4020–4024, <https://doi.org/10.1021/nl101950x>.
- [37] T. Sui, J. Dluhoš, T. Li, K. Zeng, A. Cernescu, G. Landini, A. Korsunsky, Structure-function correlative microscopy of peritubular and intertubular dentine, *Materials* 11 (9) (2018) 1493, <https://doi.org/10.3390/ma11091493>.
- [38] E. Applebaum, Incipient dental caries, *J. Dent. Res.* 12 (4) (1932) 619–627, <https://doi.org/10.1177/00220345320120040901>.
- [39] K. Momma, F. Izumi, VESTA 3 for three-dimensional visualization of crystal, volumetric and morphology data, *J. Appl. Crystallogr.* 44 (2011) 1272–1276, <https://doi.org/10.1107/S0021889811038970>.
- [40] J.M. Hughes, M. Cameron, D.C. Kevin, Structural variations in natural F, OH, and Cl apatites, *Am. Mineral.* 74 (1989) 870–876.
- [41] D. Zagorac, H. Müller, S. Ruehl, J. Zagorac, S. Rehme, Recent developments in the Inorganic Crystal Structure Database: theoretical crystal structure data and related features, *J. Appl. Crystallogr.* 52 (5) (2019) 918–925.
- [42] K.A. Galil, G.Z. Wright, Acid etching patterns on buccal surfaces of permanent teeth, *Pediatr. Dent.* 1 (1979) 230–234.
- [43] C.K. Egan, S.D.M. Jacques, M. Di Michiel, B. Cai, M.W. Zandbergen, P.D. Lee, A. M. Beale, R.J. Cernik, Non-invasive imaging of the crystalline structure within a human tooth, *Acta Biomater.* 9 (9) (2013) 8337–8345, <https://doi.org/10.1016/j.actbio.2013.06.018>.
- [44] S. Habelitz, S.J. Marshall, G.W. Marshall, M. Balooch, Mechanical properties of human dental enamel on the nanometre scale, *Arch. Oral Biol.* 46 (2) (2001) 173–183, [https://doi.org/10.1016/S0003-9969\(00\)00089-3](https://doi.org/10.1016/S0003-9969(00)00089-3).
- [45] J. Ge, F.Z. Cui, X.M. Wang, H.L. Feng, Property variations in the prism and the organic sheath within enamel by nanoindentation, *Biomaterials* 26 (16) (2005) 3333–3339, <https://doi.org/10.1016/j.biomaterials.2004.07.059>.
- [46] N. Cougot, T. Douillard, F. Dalmas, N. Pradelle, R. Gauthier, C. Sanon, B. Grosgeat, P. Colon, J. Chevalier, Towards quantitative analysis of enamel erosion by focused ion beam tomography, *Dent. Mater.* 34 (11) (2018) e289–e300, <https://doi.org/10.1016/j.dental.2018.08.304>.
- [47] O. Fejerskov, B. Nyvad, E.A.M. Kidd, Pathology of dental caries, in: O. Fejerskov, Edwina A. M. Kidd (Eds.), *Dental Caries the Disease and Its Clinical Management* Ch. 3, 19–48, 2008.
- [48] J. Reyes-Gasga, E.L. Martínez-Piñero, E.F. Brès, Crystallographic structure of human tooth enamel by electron microscopy and x-ray diffraction: hexagonal or monoclinic?, *J. Microsc.* 248 (2012) 102–109, <https://doi.org/10.1111/j.1365-2818.2012.03653.x>.
- [49] A. Thompson et al. *X-ray data booklet*, 2009.
- [50] L. Lou, A.E. Nelson, G. Heo, P.W. Major, Surface chemical composition of human maxillary first premolar as assessed by X-ray photoelectron spectroscopy (XPS), *Appl. Surf. Sci.* 254 (21) (2008) 6706–6709, <https://doi.org/10.1016/j.apsusc.2008.04.085>.
- [51] E.D. Yilmaz, J. Koldehoff, G.A. Schneider, On the systematic documentation of the structural characteristics of bovine enamel: a critic to the protein sheath concept, *Dent. Mater.* 34 (10) (2018) 1518–1530, <https://doi.org/10.1016/j.dental.2018.06.006>.
- [52] K.V. Mortimer, T.C. Tranter, A scanning electron microscopy study of carious enamel, *Caries Res.* 5 (1971) 240–263.
- [53] E. Beniash, C.A. Stiffler, C.-Y. Sun, G.S. Jung, Z. Qin, M.J. Buehler, P.U.P.A. Gilbert, The hidden structure of human enamel, *Nat. Commun.* 10 (1) (2019), <https://doi.org/10.1038/s41467-019-12185-7>.
- [54] V.P. Thompson, The tooth: an analogue for biomimetic materials design and processing, *Dent. Mater.* 36 (1) (2020) 25–42, <https://doi.org/10.1016/j.dental.2019.08.106>.



- [55] A.H. Meckel, W.J. Griebstein, R.J. Neal, Structure of mature human dental enamel as observed by electron microscopy, *Arch. Oral Biol.* 10 (5) (1965) 775–783.
- [56] J. Wilmers, S. Bargmann, Nature's design solutions in dental enamel: uniting high strength and extreme damage resistance, *Acta Biomater.* 107 (2020) 1–24, <https://doi.org/10.1016/j.actbio.2020.02.019>.
- [57] C. Lu, T. Nakamura, C.S. Korach, Effective property of tooth enamel: monoclinic behavior, *J. Biomech.* 45 (8) (2012) 1437–1443, <https://doi.org/10.1016/j.jbiomech.2012.02.016>.
- [58] Z. Xie, N.M. Kilpatrick, M.V. Swain, P.R. Munroe, M. Hoffman, Transmission electron microscope characterisation of molar-incisor-hypomineralisation, *J. Mater. Sci. Mater. Med.* 19 (10) (2008) 3187–3192, <https://doi.org/10.1007/s10856-008-3441-2>.
- [59] V. Dusevich, J.R. Melander, J.D. Eick, H. Schatten, in: *Scanning Electron Microscopy for the Life Sciences*, Cambridge University Press, Cambridge, 2012, pp. 211–235, <https://doi.org/10.1017/CBO9781139018173.014>.
- [60] P. Sutton-smith, H. Beard, N. Fazzalari, Quantitative backscattered electron imaging of bone in proximal femur fragility fracture and medical illness, *J. Microsc.* 229 (1) (2008) 60–66, <https://doi.org/10.1111/j.1365-2818.2007.01867.x>.
- [61] J.G. Skedros, R.D. Bloebaum, K.N. Bachus, T.M. Boyce, The meaning of graylevels in backscattered electron images of bone, *J. Biomed. Mater. Res.* 27 (1) (1993) 47–56, <https://doi.org/10.1002/jbm.820270107>.
- [62] J. Reyes-Gasga, J. Hémmeler, E.F. Brés, Aberration-corrected transmission electron microscopic study of the central dark line defect in human tooth enamel crystals, *Microscopy Microanalysis* 22 (5) (2016) 1047–1055, <https://doi.org/10.1017/S1431927616011648>.
- [63] J. Reyes-Gasga, E.F. Brés, Electron microscopic study of the human tooth enamel: the central dark line, in: R.A. Meyers (Ed.), *Encyclopedia of Analytical Chemistry*, John Wiley & Sons, Ltd, 2015.
- [64] J.R. Gasga, G. Carbajal-de-la-Torre, E. Brés, I.M. Gil-Chavarria, A.G. Rodríguez-Hernández, R. García-García, STEM-HAADF electron microscopy analysis of the central dark line defect of human tooth enamel crystallites, *J. Mater. Sci. Mater. Med.* 19 (2) (2008) 877–882, <https://doi.org/10.1007/s10856-007-3174-7>.
- [65] J.C. Voegel, R.M. Frank, Stages in the dissolution of human enamel crystals in dental caries, *Calcif. Tissue Res.* 24 (1) (1977) 19–27, <https://doi.org/10.1007/BF02223292>.
- [66] J.C. Voegel, R.M. Frank, Single crystal electron diffraction of normal and carious human enamel apatites, *Caries Res.* 11 (4) (1977) 189–194, <https://doi.org/10.1159/000260267>.
- [67] Y. Hayashi, High resolution electron microscopy of enamel crystallites demineralized by initial dental caries, *Scanning Microsc.* 9 (1995) 199–205, discussion 205–196.
- [68] S. Takuma, H. Tohda, N. Tanaka, T. Kobayashi, Lattice defects in and carious dissolution of human enamel crystals, *J. Electron Microsc.* 36 (1987) 387–391, <https://doi.org/10.1093/oxfordjournals.jmicro.a050645>.
- [69] H. Tohda, S. Takuma, N. Tanaka, Intracrystalline structure of enamel crystals affected by caries, *J. Dent. Res.* 66 (11) (1987) 1647–1653, <https://doi.org/10.1177/00220345870660110901>.
- [70] C. Besnard et al., Movies and dataset for: Hierarchical 2D to 3D micro/nano-histology of human dental caries lesions using light, X-ray and electron microscopy, *Mendeley Data*, V1, 2022, doi:http://dx.doi.org/10.17632/3k3syd2n3.1.
- [71] C.D. Lynch, V.R. O'Sullivan, P. Dockery, C.T. McGillicuddy, A.J. Sloan, Hunter-Schreger Band patterns in human tooth enamel, *J. Anat.* 217 (2010) 106–115, <https://doi.org/10.1111/j.1469-7580.2010.01255.x>.
- [72] E.A.M. Kidd, O. Fejerskov, What Constitutes Dental Caries? Histopathology of Carious Enamel and Dentin Related to the Action of Cariogenic Biofilms, *J. Dent. Res.* 83 (1\_suppl) (2004) 35–38.
- [73] T. Nishimura, *Histologische Untersuchungen über die Anfänge der Zahnkaries speziell der Karies des Schmelzes*, 491–545 (Buchdr. Berichthaus, 1926).
- [74] S.E.P. Dowker, J.C. Elliott, G.R. Davis, R.M. Wilson, P. Cloetens, Synchrotron X-ray microtomographic investigation of mineral concentrations at micrometre scale in sound and carious enamel, *Caries Res.* 38 (2004) 514–522, <https://doi.org/10.1159/000080580>.
- [75] G. Bergman, P. Ove Lind, A quantitative microradiographic study of incipient enamel caries, *J. Dent. Res.* 45 (5) (1966) 1477–1484, <https://doi.org/10.1177/00220345660450053701>.
- [76] A.I. Darling, Resistance of the enamel to dental caries, *J. Dent. Res.* 42 (1) (1963) 488–496, <https://doi.org/10.1177/00220345630420015601>.
- [77] C. Guzman, F. Brudevold, H. Mermagen, A soft roentgen-ray study of early carious lesions, *J. Am. Dental Assoc.* 55 (4) (1957) 509–515.
- [78] R.L. Mitchell, P. Davies, P. Kenrick, T. Volkenandt, C. Pleydell-Pearce, R. Johnston, Correlative microscopy: a tool for understanding soil weathering in modern analogues of early terrestrial biospheres, *Sci. Rep.* 11 (1) (2021), <https://doi.org/10.1038/s41598-021-92184-1>.
- [79] C. Besnard et al., Revealing the micro/nano structure and composition of human enamel caries. <https://www.postreality.io>. Poster – Augmented Reality. doi:<https://postreality.page.link/KuVvFEFwRVSMhtvW77001Z9>, 2021.
- [80] R.P. Shellis, A.S. Hallsworth, J. Kirkham, C. Robinson, Organic material and the optical properties of the dark zone in caries lesions of enamel, *Eur. J. Oral Sci.* 110 (2002) 392–395, <https://doi.org/10.1034/j.1600-0722.2002.21337.x>.
- [81] T. Abdelrehim, M. Salah, L. Sailer, H.P. Chew, Identification of demineralization zones in early enamel decay based on image correlation between scanning electron microscope (SEM) and optical coherence tomography (OCT), in: *European Conferences on Biomedical Optics 2021 (ECBO)*, ETu2A.41 (Optical Society of America, Munich, 2021).
- [82] H. Deyhle, S.N. White, O. Bunk, F. Beckmann, B. Müller, Nanostructure of carious tooth enamel lesion, *Acta Biomater.* 10 (1) (2014) 355–364, <https://doi.org/10.1016/j.actbio.2013.08.024>.
- [83] P.D. Nellist, The Principles of STEM Imaging, in: Stephen J. Pennycook, Peter D. Nellist (Eds.), *Scanning Transmission Electron Microscopy: Imaging and Analysis*, Springer New York, New York, NY, 2011, pp. 91–115, [https://doi.org/10.1007/978-1-4419-7200-2\\_2](https://doi.org/10.1007/978-1-4419-7200-2_2).
- [84] J.F. Ziegler, M.D. Ziegler, J.P. Biersack, SRIM – The stopping and range of ions in matter (2010), *Nucl. Instrum. Methods Phys. Res., Sect. B* 268 (11–12) (2010) 1818–1823, <https://doi.org/10.1016/j.nimb.2010.02.091>.
- [85] T. Scientific, User's guide Avizo software 2019, 2019.
- [86] R.C.G. De Medeiros, J.D. Soares, F.B. De Sousa, Natural enamel caries in polarized light microscopy: differences in histopathological features derived from a qualitative versus a quantitative approach to interpret enamel birefringence, *J. Microsc.* 246 (2012) 177–189, <https://doi.org/10.1111/j.1365-2818.2012.03609.x>.
- [87] L.M. Silverstone, Laboratory studies on the demineralization and remineralization of human enamel in relation to caries mechanisms, *Aust. Dent. J.* 25 (1980) 163–168, <https://doi.org/10.1111/j.1834-7819.1980.tb03707.x>.
- [88] O. Ronneberger, P. Fischer, T. Brox, U-Net: convolutional networks for biomedical image segmentation, III, *Springer International Publishing, Munich, Germany*, 2015, pp. 234–241.
- [89] O. Ronneberger, P. Fischer, T. Brox, U-Net: convolutional networks for biomedical image segmentation, *arXiv:1505.04597*, 1–8 (2015).
- [90] E. Franken, M. van Almsick, P. Rongen, L. Florack, B. ter Haar Romeny, An efficient method for tensor voting using steerable filters, in: Aleš Leonardis, Horst Bischof, Axel Pinz (Eds.), *Computer Vision – ECCV 2006. Lecture Notes in Computer Science*, vol. 3954, Springer, Berlin, Heidelberg, pp. 228–240, 2006.
- [91] J.D. Arregui-Mena, P.D. Edmondson, A.A. Campbell, Y. Katoh, Site specific, high-resolution characterisation of porosity in graphite using FIB-SEM tomography, *J. Nucl. Mater.* 511 (2018) 164–173, <https://doi.org/10.1016/j.jnucmat.2018.08.047>.
- [92] F. de la Peña et al., hyperspy/hyperspy: Release v1.7.0 (v1.7.0), (Zenodo) (2022), <https://doi.org/10.5281/zenodo.592838>.
- [93] C. Rau, Imaging with coherent synchrotron radiation: X-ray Imaging and Coherence Beamline (I13) at Diamond Light Source, *Synchrotron Radiation News* 30 (5) (2017) 19–25, <https://doi.org/10.1080/08940886.2017.1364530>.
- [94] C. Rau et al., Micro- and nano-tomography at the DIAMOND beamline I13L imaging and coherence, in: B. Müller, G. Wang, *SPIE Optical Engineering + Applications - Developments in X-Ray Tomography XI*, Volume Proc. of SPIE 10391 103910T-103911-103918, SPIE, San Diego, California, United States, 2017.
- [95] C. Rau, U. Wagner, Z. Pešić, A. De Fanis, Coherent imaging at the Diamond beamline I13, *Phys. Status Solidi (a)* 208 (11) (2011) 2522–2525.
- [96] N. Wadeson, M. Basham, Savu: a Python-based, MPI framework for simultaneous processing of multiple, N-dimensional, large tomography datasets. *arXiv preprint arXiv:1610.08015*, 10 (2016).
- [97] R.C. Atwood, A.J. Bodey, S.W.T. Price, M. Basham, M. Drakopoulos, A high-throughput system for high-quality tomographic reconstruction of large datasets at Diamond Light Source, *Philos. Trans. Roy. Soc. A: Math. Phys. Eng. Sci.* 373 (2043) (2015) 20140398.
- [98] M. Basham, J. Filik, M.T. Wharmby, P.C.Y. Chang, B. El Kassaby, M. Gerring, J. Aishima, K. Levik, B.C.A. Pulford, I. Sikhariulidze, D. Sneddon, M. Webber, S.S. Dhesi, F. Maccherozzi, O. Svensson, S. Brockhauser, G. Náráy, A.W. Ashton, Data Analysis Workbench (DAWN), *J. Synchrotron Radiation* 22 (3) (2015) 853–858, <https://doi.org/10.1107/S160057751500228310.1107/S1600577515002283/fv5032sup1.pdf>.
- [99] W.S. Rasband, ImageJ, U. S. National Institutes of Health, Bethesda, Maryland, USA, 1997–2018, <https://imagej.nih.gov/ij/>.
- [100] J. Schindelin, I. Arganda-Carreras, E. Frise, V. Kaynig, M. Longair, T. Pietzsch, S. Preibisch, C. Rueden, S. Saalfeld, B. Schmid, J.-Y. Tinevez, D.J. White, V. Hartenstein, K. Eliceiri, P. Tomancak, A. Cardona, Fiji: an open-source platform for biological-image analysis, *Nat. Methods* 9 (7) (2012) 676–682, <https://doi.org/10.1038/nmeth.2019>.